Geomagnetic jerk features produced using synthetic core flow models

K.J. Pinheiro, Hagay Amit, Filipe Terra-Nova

Geomagnetic jerk features **produced using** synthetic core flow models

K. J. Pinheiro[1,2], H. Amit[2], F. Terra-Nova[2,3]

March 6, 2019

[1] *Observatório Nacional, Geophysics Department, Rio de Janeiro, CEP:20921-400, Brazil. E-mail: kpinheiro@on.br*

[2] *CNRS, Université de Nantes, Nantes Atlantiques Universités, UMR CNRS 6112, Laboratoire de Planétologie et de Géodynamique, 2 rue de la Houssinière, F-44000 Nantes, France.*

[3] *Departamento de Geofísica, Instituto de Astronomia, Geofísica e Ciências Atmosféricas, Universidade de São Paulo, Rua do Matão, 1226, 05508-090, São Paulo, Brazil.*

Abstract

Geomagnetic jerks are the shortest temporal variations of the magnetic field generated in the Earth's core. The physical mechanism producing such abrupt changes as well as their spatio-temporal characteristics are not well understood. In order to explore geomagnetic jerk' generation and their characteristics, we use a set of synthetic core flow models to solve the radial magnetic induction equation. We analyze changes of trend in the secular variation time series using a **cubic** polynomial fit, by invoking a new formalism of jerk amplitude per unit duration time. A new visualization scheme allows interpretating **jerk amplitudes** and occurrences in space and time. We find that a mild time-dependence of flow amplitude, while keeping a fixed pattern, reproduces geomagnetic jerk amplitudes. The polynomial fits were compared with two line-segments fits at ten sampled magnetic observatories about historical jerk occurrences. The differences between the misfits in the two approaches are small, which may question the definition of geomagnetic jerks as sharp "V-shape". The local time series in our models exhibit **secular acceleration** changes of sign that reproduce some main observed characteristics of geomagnetic jerks: (i) a range of amplitudes that encompass those observed in geomagnetic jerks, (ii) non-simultaneous occurrence, (iii) non-global occurrence, (iv) spatial variability of amplitudes and (v) strongest amplitudes in the radial component.

Keywords: magnetic field, geomagnetic jerks, core flows, secular variation, secular acceleration.

1 Introduction

The geomagnetic field generated in the outer core varies on a wide range of timescales, from the geomagnetic secular variation (SV) over months to hundreds of years, to paleomagnetic SV over longer timescales such as reversals that last thousands of years to chrons that last hundreds of thousands of years (Merrill et al., 1996). Abrupt changes of the SV termed "geomagnetic jerks" represent the shortest observed timescales of the core field. A jerk is classically defined as a "V-shape" of the geomagnetic SV (e.g. Courtillot et al., 1978; Malin and Hodder, 1982; Bloxham et al., 2002; Alexandrescu et al., 1996; Chambodut and Mandea, 2005; Michelis and Tozzi, 2005; Pinheiro et al., 2011) or equivalently as **an abrupt** change in the secular acceleration (SA) (e.g. Huy et al., 1998; Chambodut et al., 2007; Mandea et al., 2010). Alternatively, if the SA change is indeed abrupt, a jerk can be defined based on spectral properties as a non-differentiable second time derivative of a magnetic field component (Gillet et al., 2013). **Here we define a jerk as any change of sign in the SA. We do not consider same-sign changes in SV trends because such time series correspond to much weaker events of** $2\ nT/yr^2$ **amplitude difference at most, possibly much less.**

In the twentieth century, jerks with different spatio-temporal characteristics were reported: the 1901, 1913, 1925 (Alexandrescu et al., 1996), 1969, 1978 (Huy et al., 1998; Mandea et al., 2010; Pinheiro et al., 2011; Brown et al., 2013), 1991 (De Michelis et al., 1998; Michelis et al., 2000; Nagao et al., 2003; Chambodut and Mandea, 2005) and 1999 (Mandea et al., 2000) jerks were detected over worldwide surface observatories while the 1932 was locally observed (Alexandrescu et al., 1996). Since 2000, the Earth's magnetic field has been continuously measured by satellites that provide excellent spatial data coverage and thus significantly improve global geomagnetic field and SV models, as well as mapping of SA which provides insight for the understanding of jerks. Jerks were observed using satellite data in 2003 (Olsen and Mandea, 2007), 2005 (Olsen and Mandea, 2008), 2007 (Chulliat et al., 2010; Olsen et al., 2009), 2009 and 2011 (Chulliat and Maus, 2014) and 2014 (Torta et al., 2015; Kotzé, 2017; Soloviev et al., 2017). Unlike the historical jerks, the recent satellite era jerks are non-global. For example, the 2003 jerk was only observed in an area around longitude 90^oE and latitudes $\pm\ 30^o$ (Olsen and Mandea, 2008). Another interesting feature of jerks is their non-simultaneity, i.e. the same event is observed in different times at different observatories. For example, the 1969 and 1978 jerks appear in the southern hemisphere with a delay of about two years (Alexandrescu et al., 1996). Finally, geomagnetic jerks have different amplitudes for different SV components (Brown et al., 2013).

Several methods for detecting jerk time occurrences and quantifying their amplitudes have been explored in the past few decades: fitting of two line-segments to the SV (Mouël et al., 1982; Huy et al., 1998; De Michelis et al., 1998; Michelis et al., 2000; Olsen and Mandea, 2007; Pinheiro et al., 2011; Brown et al., 2013), piecewise quadratic models **to the geomagnetic field** (Stewart and Whaler, 1995), wavelet analysis (Alexandrescu et al., 1995, 1996; Michelis and Tozzi, 2005; Chambodut and Mandea, 2005) and by **entropy methods applied to the geomagnetic field time series (Balasis et al., 2016)**. **The identification of jerks is**

performed using e.g. monthly means data to remove the external field (e.g. Brown et al., 2013).

The existence of geomagnetic jerks as well as their spatio-temporal characteristics may originate from either a uniform and simultaneous signal generated at the core-mantle boundary (CMB) that is distorted by the electrically-conducting mantle (Backus, 1983; Alexandrescu et al., 1999; Nagao et al., 2003; Pinheiro and Jackson, 2008), or from a non-uniform and non-simultaneous signal generated at the CMB (Maus et al., 2008; Silva and Hulot, 2012) that is not distorted by an assumed insulating mantle, or a combination of the two effects. For example, differential delays of geomagnetic jerks were linked to the mantle conductivity (Pinheiro and Jackson, 2008; Pinheiro et al., 2015). In contrast, the dynamical origin of geomagnetic jerks was linked to core flow acceleration patterns (Huy et al., 1998; Wardinski et al., 2008) such as torsional oscillations (Bloxham et al., 2002) or more complex waves (Dormy and Mandea, 2005). Bloxham et al. (2002) fitted a steady flow superimposed by a time-varying wave-like flow to reproduce geomagnetic jerks by torsional oscillations. Silva and Hulot (2012) analysed the 2003 jerk and concluded that it was caused by a more complex phenomena than simple torsional oscillations. Cox et al. (2014) developed a forward model of torsional oscillations which was later applied to a steady background magnetic field to solve the magnetic induction equation (Cox et al., 2016). They obtained smoothly varying SV time series that somewhat differ from the classical "V-shape" of the jerks. Overall, these studies did not fully reproduce the main spatio-temporal characteristics of jerks such as jerk delay times, global vs. local patterns and "V-shape" SV trends. The physical mechanism that may produce such abrupt field variations therefore remains an outstanding issue in geomagnetism.

Because a jerk is defined as a change of sign in the SA, jerk kinematics is governed by the time derivative of the radial induction equation. The radial component of the induction equation just below the CMB (where the radial velocity vanishes) is:

$$\dot{B}_r + \mathbf{u}_h \cdot \nabla_h B_r + B_r \nabla_h \cdot \mathbf{u}_h = \lambda \left(\frac{1}{r^2} \frac{\partial^2}{\partial r^2} (r^2 B_r) + \nabla_h^2 B_r \right), \tag{1}$$

where B_r is the radial magnetic field, dot over symbol denotes time derivative, $\mathbf{u}_h$ is the velocity tangential to the CMB surface, λ is the magnetic diffusivity, r is the radial coordinate, and ∇_h is the tangential part of the vector differentiation operator. The second term on the left hand side of (1) is magnetic field advection by the tangential flow, the third term is magnetic field stretching by downwellings and upwellings and the two terms on the right hand side represent respectively radial and tangential magnetic diffusion due to the core fluid finite electrical conductivity.

Magnetic induction is characterized by the ratio of magnetic field generation by the flow to its dissipation by diffusion (1) and is represented by the magnetic Reynolds number

$$Rm = \frac{UL}{\lambda} \tag{2}$$

where U and L are typical flow and length scales, respectively. For the Earth's core $U \sim 5 \cdot 10^{-4}$ m/s, $L \sim 1000$ km (Holme, 2015) and $\lambda \sim 0.5 - 1$ m^2/s (Poirier, 2000;

Pozzo et al., 2012), giving $Rm = 500 - 1000$. This large Rm estimate supports neglecting magnetic diffusion for short-term core kinematics (e.g. Roberts and Scott, 1965).

The time derivative of (1) in the frozen-flux limit, i.e. where diffusion is negligible, is given by (e.g. Silva and Hulot, 2012)

$$\ddot{B}_r = -\dot{\mathbf{u}} \cdot \nabla_h B_r - B_r \nabla_h \cdot \dot{\mathbf{u}} - \mathbf{u} \cdot \nabla_h \dot{B}_r - \dot{B}_r \nabla_h \cdot \mathbf{u} \tag{3}$$

According to (3) the SA (left hand side) is induced by the interaction of the field with the flow acceleration (first two terms on the right hand side) and by the interaction of the SV with the flow (last two terms on the right hand side). Previous studies found that steady flows cannot explain the SA, i.e. the first two terms on the right hand side of (3) dominate over the last two (Bloxham et al., 2002; Silva and Hulot, 2012; Cox et al., 2016).

Silva and Hulot (2012) explored a joint inversion of the SV and SA based on (1) and (3). They showed that core flow acceleration cannot be purely toroidal. For the 2003 jerk they found a drastic temporal change in the flow acceleration (size and direction) in the eastern hemisphere. Cox et al. (2016) adopted the forward approach to evaluate the effects of the complexity of the background magnetic field morphology (or field roughness) on the sensitivity of jerks to zonal core flows. They concluded that the field morphology may explain local jerks, without necessarily a need for small scale core flows, as was previously argued by Bloxham et al. (2002). However Cox et al. (2016) showed that not all parts of the Earth's magnetic field are equally sensitive to zonal flow acceleration hence the difficulty to obtain global jerks with such dynamics. By taking advantage of high resolution numerical dynamo simulations with a very low Ekman number (Aubert et al., 2017; Schaeffer et al., 2017), Aubert (2018) found that quasi-geostrophic Alfvén waves cause short, intermittent and strong energy pulses of SA at the equatorial belt, which may **be** the origin of geomagnetic jerks there.

In this study we first **explore** the SA produced by steady flows. Although previous studies, such as Bloxham et al. (2002), have already shown that geomagnetic jerks are not produced by steady flows, we show that field roughness alone produces changes of sign in the SA and we quantify the spatio-temporal characteristics of these events. We then **add** a mild time-dependence to the flow amplitude in order to reproduce the main features observed in the geomagnetic jerks, in particular their amplitudes.

In order to explore the kinematic origin of geomagnetic jerks and their spatio-temporal characteristics, we **calculate** the interaction of synthetic flow models with an initial geomagnetic field model on the CMB. **This approach allows to reveal the potential of each flow component to generate jerks, and as such provides fundamental information on the core dynamics that produce jerks.** Each flow model has a steady pattern. The flow amplitude is either steady, or characterized by a simple periodic time dependence. We forward **solve** the radial magnetic induction equation and upward **continue** the radial field to the Earth's surface to produce time series of field components and their SV. The SV time series **are** analysed in terms of jerk densities and amplitudes. For comparison we **apply** the same analysis to some SV time series from the available dataset of surface observatories during the occurrences of geomagnetic jerks.

2 Method

2.1 Synthetic core flow models

The fluid motion **just below the CMB** is generically written as a sum of toroidal and poloidal parts represented by their respective potentials Ψ and Φ

$$\mathbf{u}_h = \nabla \times \Psi \hat{r} + \nabla_h \Phi \tag{4}$$

or,

$$\mathbf{u}_h = \frac{1}{r}\left[\left(\frac{1}{\sin\theta}\frac{\partial \Psi}{\partial \phi} + \frac{\partial \Phi}{\partial \theta}\right)\hat{\theta} - \left(\frac{\partial \Psi}{\partial \theta} - \frac{1}{\sin\theta}\frac{\partial \Phi}{\partial \phi}\right)\hat{\phi}\right] \tag{5}$$

where r is the radial coordinate, θ is co-latitude and ϕ is longitude. The corresponding unit vectors are $\hat{r}$, $\hat{\theta}$ and $\hat{\phi}$, respectively. For fundamental intuition we considered a set of ten single spherical harmonic flow models $\Psi = \alpha \mathcal{T}_\ell^{mx}$ or $\Phi = \alpha \mathcal{P}_\ell^{mx}$ where α is the flow amplitude, ℓ is degree, m is order and x is c or s denoting cosine or sine respectively. The toroidal potential $\mathcal{T}$ represents a non-divergent flow which can be described by a streamfunction, whereas the poloidal potential $\mathcal{P}$ represents a 2D divergent flow composed of surface sources and sinks (or upwellings and downwellings). The flow models are from Huguet and Amit (2012) including one additional model ($\mathcal{T}_3^0$). These models encompass a variety of flow morphologies, including toroidal and poloidal, equatorially symmetric and asymmetric, zonal and non-zonal.

We first explore steady flow models in order to test how field **and consequently SV** roughness may produce changes in sign of SA. We will show that these steady flows yield too weak amplitudes of the change of sign in SA, as was previously found (Bloxham et al., 2002; Silva and Hulot, 2012). We therefore next introduce mild time-dependence to the flow amplitude which is set to oscillate without changing its sign. In the time-dependent flow models the **spatial** pattern is fixed but the amplitude α varies with time as follows:

$$\alpha(t) = \alpha_0 \left(1 + \frac{1}{4}\cos\omega t\right) \tag{6}$$

where α_0 is the steady flow amplitude, ω is the frequency and t is time. For comparison purposes, in all models the amplitude α_0 was set so that the rms velocity is $\sqrt{\int_{S_c} \mathbf{u_h}\cdot\mathbf{u_h} dS_c} = 15$ km/yr (where S_c is the CMB surface and $dS_c = R_c^2 sin\theta d\theta d\phi$ is a **CMB** surface increment, where R_c is **the core radius**), on the order of estimated large-scale core flow magnitude (Finlay and Amit, 2011; Holme, 2015). The factor $\frac{1}{4}$ in the time-dependent part of (6) corresponds to **the relative** time-dependence of core flow magnitude estimates (Amit and Olson, 2006; Finlay and Amit, 2011). The frequency ω in (6) corresponds to a period of $T = 50$ yrs which is roughly the period of **slow torsional (or MAC) waves motivated by the observed period of** axial dipole variability (Buffett, 2014) **in the gufm1 field model (Jackson et al., 2000)**. We also tested a higher frequency corresponding to $T = 5$ yrs which roughly corresponds to **small amplitude waves associated with** length of day variation periodicity (Gillet et al.,

2010). However, we found that such high frequency results in high frequency jerks that are difficult to characterize. From hereafter we will use the term time-dependent models for these semi-steady synthetic flows in which the **spatial** pattern is steady but the amplitude varies periodically with time without changing sign as prescribed by (5).

2.2 Synthetic magnetic secular variation time series

The synthetic magnetic SV at the CMB is calculated from the interaction of the synthetic core flow models with a geomagnetic field model. The time series of the radial magnetic field B_r at the CMB are obtained by time iteration of the radial magnetic induction equation just below the CMB using a finite differences method. For initialization we arbitrary chose the geomagnetic field model CM4 (Sabaka et al., 2004) in 1969 (Fig. 1). For comparison, we also used exclusively its dipole component.

We iterate B_r in time using

$$B_r(t_{i+1}) = B_r(t_i) + \dot{B}_r(t_i)\Delta t \tag{7}$$

where t is time, i denotes the iteration step and $\Delta t = 1$ day is the time step. **We neglect the generally unknown radial magnetic diffusion term, while we retain tangential magnetic diffusion for numerical stability.** We therefore solve

$$\dot{B}_r + \mathbf{u}_h \cdot \nabla_h B_r + B_r \nabla_h \cdot \mathbf{u}_h = \lambda \nabla_h^2 B_r \tag{8}$$

In most cases we consider λ values that correspond to $Rm = 1000$ and for comparison two additional models with $Rm = 500$ are examined.

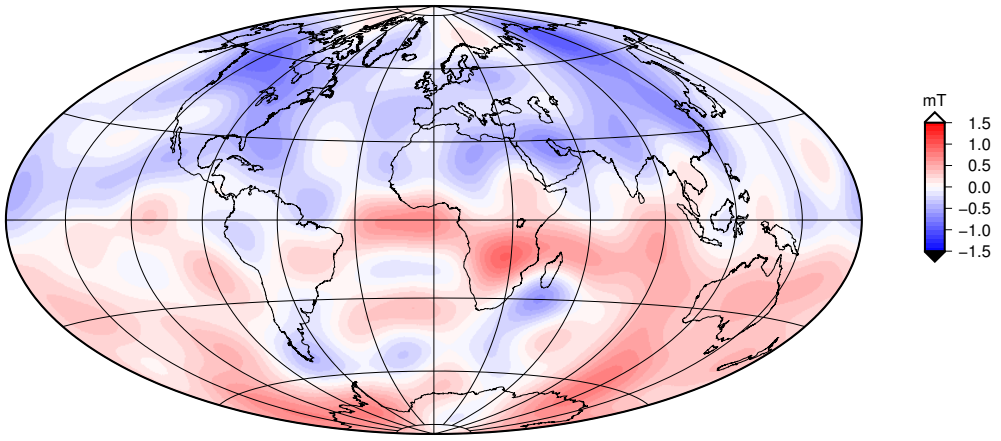

Figure 1: Radial geomagnetic field B_r at the CMB expanded until spherical harmonic degree and order 14 based on the CM4 model in 1969 (Sabaka et al., 2004).

Because the models are run in physical space rather than the commonly used spectral space (e.g. Cox et al., 2016), the radial component of the magnetic field at the CMB is upward

continued as a potential field using the appropriate kernels **(Gubbins and Roberts, 1987; Johnson and Constable, 1997; Gubbins, 2004; Constable, 2007; Terra-Nova et al., 2017)** to obtain the three components of the vector field at the Earth's surface. We then calculated the time series of the first time derivatives (SV) of the three field components $\dot{B}_r$, $\dot{B}_\theta$ and $\dot{B}_\phi$ at the Earth's surface.

2.3 Detection and characterization of jerks

Here we describe step-by-step the procedure to detect and characterize jerks: (i) determination of occurrence times by finding SA changes of sign, (ii) determination of time windows, (iii) fitting third order polynomials to the SV time series and (iv) calculating jerk amplitudes per duration time.

A $2^\circ \times 2^\circ$ regular grid in co-latitude and longitude was used as a mesh of **synthetic** observatories on the surface of the Earth **(as in Mandea and Olsen, 2006; Olsen and Mandea, 2007, 2008, i.e. analogous though not identical to virtual observatories)** to detect and characterize changes in sign in SA. **As a first step the** occurrence times t_0 of magnetic jerks at any grid point were detected by searching for changes of sign in the SA at the surface, even though some of these changes do not correspond to the amplitudes observed in geomagnetic jerks.

In the second step we determine the time windows for the jerk analysis. Our choice of a time window to analyze an individual jerk is set by **two** considerations. **First, for** a meaningful fit with sufficient points, we require a minimum of three years before and after t_0. **Second, incorporating a** transition between two same-sign SV trends, which corresponds to a change of sign in the third time derivative of the field (or a transition of the SV curve from concave to convex or vice-versa), might render the low order polynomial fit **inadequate**. Therefore such a transition delimits the time window for the analysis of an individual jerk. **Overall, in all cases the time window is delimited on both sides by either a change of sign in the third time derivative or an edge of the simulation period.**

In the third step we fit a third order polynomial to the SV at the determined time window:

$$\dot{B}_j = at^3 + bt^2 + ct + d, \tag{9}$$

where j represents any field component. This polynomial fit for each SA change of sign expresses the two trends of the time series before and after the jerk occurrence in terms of a single function. It is motivated **primarily** by the smooth nature of the synthetic SV time series in our models. **Some analyses of observatory data indeed found no evidence of a discontinuity in SA at jerk times (Holme and de Viron, 2013; Cox et al., 2018).** We chose a third order because it is the lowest order (i.e. simplest) expansion that allows for SV time series to be non-linear and asymmetric around t_0.

Fig. 2 illustrates the procedure for characterizing jerks in the synthetic time series. The black crosses represent the simulated values and the red curve the polynomial fit **to the**

SV (Fig. 2 top). The blue arrow indicates the occurrence time when the SA is zero (Fig. 2 middle). The **green** arrow indicates a time when there is a change of sign in the third time derivative **(Fig. 2 bottom)**. In this case the fitting window is from the third time derivative change of sign to the last data point (interval between **the green arrow and the end of the time series** in Fig. 2).

As a final step we calculate the amplitude per duration time. The jerk amplitude $\mathcal{A}$ around the occurrence time t_0 when the SA is zero is given by the absolute value of the difference between the SA at times $t_0 - \frac{\mathcal{D}}{2}$ and $t_0 + \frac{\mathcal{D}}{2}$, where $\mathcal{D}$ is the jerk duration period (Nagao et al., 2003). The SA is given by

$$\ddot{B}_j = 3at^2 + 2bt + c, \tag{10}$$

therefore

$$\mathcal{A} \equiv |\ddot{B}_j(t_0 + \mathcal{D}/2) - \ddot{B}_j(t_0 - \mathcal{D}/2)| = \mathcal{D}|6at_0 + 2b| \tag{11}$$

The jerk occurrence time is expressed in terms of the polynomial coefficients by equating the SA (10) to zero:

$$t_0 = \frac{-b \pm \sqrt{b^2 - 3ac}}{3a} \tag{12}$$

Substituting t_0 (12) into (11) finally gives:

$$\mathcal{A} = |\ddot{B}_j(t_0 + \mathcal{D}/2) - \ddot{B}_j(t_0 - \mathcal{D}/2)| = 2\mathcal{D}\sqrt{b^2 - 3ac} \tag{13}$$

or

$$\frac{\mathcal{A}}{\mathcal{D}} = 2\sqrt{b^2 - 3ac}. \tag{14}$$

In this approach $\mathcal{D}$ **is a running time variable and the amplitude** $\mathcal{A}$ is time-dependent **but the ratio** $\mathcal{A}/\mathcal{D}$ **is fixed for a given jerk**. We therefore calculated the jerk amplitude per unit duration time $\mathcal{A}/\mathcal{D}$ which only depends on the polynomial fit coefficients (14). When $b^2 - 3ac < 0$ the SA does not change sign, therefore it is not possible to identify jerks in our polynomial approach. Fig. 3 shows examples of the quantification of jerk **amplitude per unit duration time** in two time series: in the first location there is only one event (blue line) and in the second location there are two events (red/green lines). The fits are very good despite the different number of data points around the occurrence times. The fits capture a large factor $\sim$ 10 of **amplitude per unit duration time** difference between these jerks (blue vs. red/green lines), which is independent of duration period as mentioned above.

As noted above, in our approach $\mathcal{D}$ is used as a running time variable, which is analogous but not identical to the jerk duration period of Nagao et al. (2003) who defined $\mathcal{D}$ as a fixed period of non-linear SV around the occurrence time. Outside this period the amplitude is constant (Nagao et al., 2003), in contrast to our time-dependent amplitude. Nevertheless, for convenience from hereafter we refer to $\mathcal{D}$ as a duration time, bearing in mind its conceptual difference to the quantity originally defined by Nagao et al. (2003).

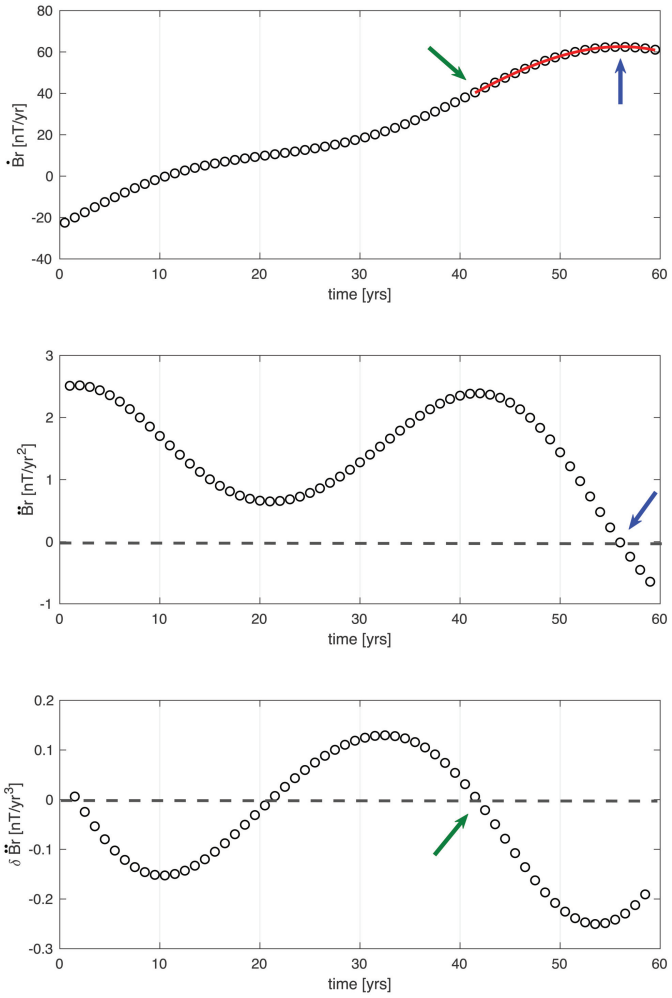

Figure 2: **Example of a third order polynomial fit applied to the results of the radial component of the time-dependent flow model $\mathcal{T}_1^0(t)$ at a given location. The black circles are the model for the SV (top), SA (middle) and third time derivative (bottom). The red line (top) is the polynomial fit, the blue arrow (top and middle) indicates the jerk occurrence time t_0 where the SA crosses zero and the green arrow (top and bottom) delimits the time window where the third time derivative crosses zero.**

In order to exclude very weak jerks that are typically ignored in the analysis of geomagnetic data (sometimes termed "blind zones", see Chambodut and Mandea, 2005), we report in Tables 1 and 2 the statistics above certain amplitude **per unit duration time** thresholds. **For each**

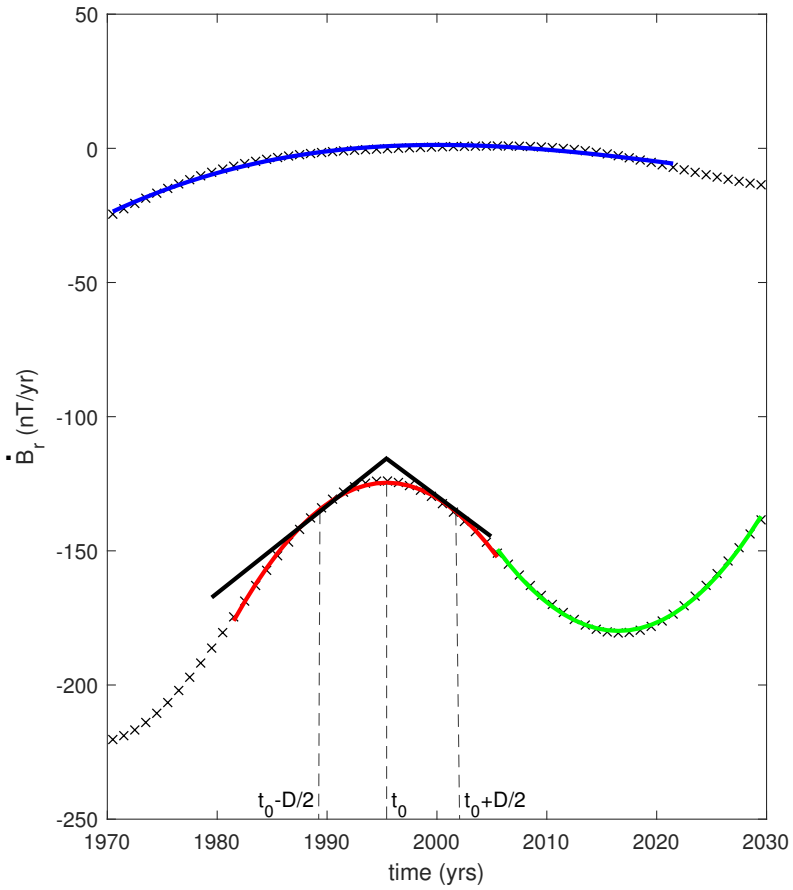

Figure 3: Two examples of time series at two different locations both obtained from the time-dependent $\mathcal{T}_1^0(t)$ model (black crosses). The blue line is the third order polynomial fit to a weak jerk with $\mathcal{A}/\mathcal{D} = 0.04$ nT/yr^3. The red and green lines are the polynomial fits to time series where two jerks occur with $\mathcal{A}/\mathcal{D} = 0.50$ nT/yr^3 and $\mathcal{A}/\mathcal{D} = 0.53$ nT/yr^3, respectively. The black straight-lines illustrate the SV slopes of the red curve fit for an arbitrary duration $\mathcal{D}$.

model and each component, we arbitrarily chose to account for jerks stronger than one fourth and one half of the maximum amplitude ($< \mathcal{A}/\mathcal{D}(max/4) >$ and $< \mathcal{A}/\mathcal{D}(max/2) >$ respectively, where $<>$ denotes the mean in space and time for each flow model and SV component. In addition, for comparison with the strongest observed geomagnetic jerks (Tables 3-4), we also report in Tables 1-2 the maximum amplitude ($\mathcal{A}/\mathcal{D}$ (max)) for each flow model and SV component.

Jerk density was calculated by the relative surface area per unit time at which jerks were

detected at each model:

$$\rho = \frac{1}{\tau}\frac{1}{S}\int_{\tau}\int_{S}\delta(\theta,\phi)dSdt \tag{15}$$

where τ **is the period of analysis,** S **is the Earth's surface,** $dS = R^2 \sin\theta d\theta d\phi$ **is Earth's surface increment where** R **is Earth's surface radius,** $\delta(\theta,\phi) = 0$ when there is no jerk and $\delta(\theta,\phi) = 1$ when a jerk is detected at **an** observatory located at (θ,ϕ). The duration over which we search for magnetic jerks is τ=60 years. A test of statistical robustness was performed by considering a longer run with τ=100 years. When several magnetic jerks occur in the same location at different times they are counted several times for the jerk density calculation.

In order to characterize the observed geomagnetic jerks at surface observatories, we applied both the method of two line-segments (Stewart and Whaler, 1995; Huy et al., 1998; Chambodut and Mandea, 2005; Pinheiro et al., 2011) as well as third order polynomial fits. For the polynomial fits we applied the exact same procedure as for the SV time series from the simulations. For the two line-segments we followed the method proposed by Pinheiro et al. (2011):

$$\dot{B}_j(t) = a_1(t - t_0) + b \tag{16}$$

for $t \leq t_0$ and

$$\dot{B}_j(t) = a_2(t - t_0) + b \tag{17}$$

for $t \geq t_0$ where $\dot{B}_j$ denotes a geomagnetic component, t_0 is the time intersection of the two line-segments which define the jerk occurrence time, the jerk amplitudes are given by the absolute difference between the two slopes $|a_1 - a_2|$ and b is the SV at the occurrence time. We calculated the model parameters (a_1, a_2 and b) for all t_0 at intervals of 0.001 yr. The misfit of each method (two line-segments or polynomial) is defined by:

$$\sigma = \sqrt{\frac{\sum_N (\dot{B}_j^{obs} - \dot{B}_j^{fit})^2}{N}} \tag{18}$$

where $\dot{B}_j^{obs}$ is the observed SV of component j, $\dot{B}_j^{fit}$ is its straight-lines or polynomial fit and N is the number of data points. **The same time window, i.e. the same value of** N**, is used for both fits, line-segments and polynomial.** The best-fit value for t_0, at each observatory and for each field component, is chosen by minimizing the misfit. When the minimum misfit is in one of the extremes of the time series, it is not possible to identify jerks so these cases are classified as "non-detected" jerks (see Fig. 2 of Pinheiro et al., 2011). In addition, we exclude same-sign **changes** of geomagnetic SA **which are weaker than those exhibiting changes of sign**.

2.4 Jerks visualization scheme

We developed a novel scheme to visualize the spatio-temporal distribution of magnetic jerks, which includes both the occurrence times and the absolute amplitudes per unit du-

ration. In Figs. 6-8 and 10-12 circles represent the first jerk event while (rather rare) diamonds represent a possible second event at the same location. The color of each symbol indicates the time when the jerk appears while its size indicates the absolute amplitude per unit duration (in nT/yr^3). Symbol sizes are divided into three ranges of absolute $\mathcal{A}/\mathcal{D}$ values, calculated for each specific model and for each component.

The visualisation scheme is most effective when a single event is observed over the analyzed period at a given location (only one circle, no superimposed diamonds). Our models give roughly one jerk each $T/2 = 25$ years at a given location, where T is the period of the time-dependent amplitude. For this reason we limited our visualisation to a shorter 15-years time window.

3 Results

3.1 Simulated magnetic jerks

We calculated SV time series obtained from the steady and time-dependent flow models in order to explore SA changes of sign. The results are summarized in Tables 1 and 2 for the ten steady and time-dependent flow models, respectively. For each flow model and each magnetic field component we reported jerk densities ρ and amplitudes per unit duration **time** $\mathcal{A}/\mathcal{D}$. For comparison among the models we mostly refer to the $< \mathcal{A}/\mathcal{D}(max/4) >$ values that are calculated without jerks weaker than one fourth of the maximum **amplitude per unit duration time**. A stronger threshold $< \mathcal{A}/\mathcal{D}(max/2) >$ is also applied to test the sensitivity of the results to the choice of "blind zone" threshold. In addition, we refer to the maximum values (Tables 1-2) which may possibly correspond to the amplitude values at years when geomagnetic jerks were reported (Tables 3-4). For the statistics we considered 60 years of analysis, while for plotting jerk maps from time-dependent models we considered a narrower time window in order to avoid multiple occurrences at the same location which renders difficult the interpretation of differential delay times.

We start with the simple toroidal $\mathcal{T}_1^0$ and $\mathcal{T}_1^0(t)$ steady **and time-dependent flows**, corresponding to solid body rotation in the east direction, to validate the calculations and to gain some **insight about the influence of flow geometry. Six** additional models were tested with these flow models. First, the results for two magnetic Reynolds numbers ($R_m = 500$ and 1000) are practically identical (Tables 1-2), demonstrating that diffusion does not affect the solutions of our models. For all other flow models we used $Rm = 1000$. Second, the **results** with a purely dipolar initial magnetic field resulted in much weaker changes of SA at the Earth's surface demonstrating the possible importance of small-scale field in the generation of jerks. For all other flow models we used the field model expanded to degree and order 14 (Fig. 1) for initialization. Third, we compared results obtained with two different simulation times of 60 and 100 years. We observed practically identical values of mean jerk **amplitude per unit**

duration time, indicating that 60 years is sufficiently long for meaningful statistics (Tables 1-2).

The synthetic steady and time-dependent flow models produced magnetic jerks spanning a range of **amplitudes per unit duration time** and densities (Tables 1 and 2). Several general findings are worth noting. For almost all steady and time-dependent flow models, jerk **amplitudes per unit duration time** are largest in the r component. The largest maximum jerk amplitude per unit duration in the steady models is observed for the r component in $\mathcal{T}_3^0$ ($\mathcal{A}/\mathcal{D}(max) \sim 0.16\ nT/yr^3$), while in the time-dependent models it is observed for the r component in $\mathcal{P}_2^0(t)$ ($\mathcal{A}/\mathcal{D}(max) \sim 3.4\ nT/yr^3$). Based on $< \mathcal{A}/\mathcal{D}(max/4) >$, mean jerk **amplitudes per unit duration time** in the r component are 80-150% larger than the mean θ and ϕ components (Tables 1-2). On average the jerk **amplitudes per unit duration time** in the time-dependent models exceed those of the steady flow models by more than an order of magnitude (Tables 1-2).

Overall, among all time-dependent models and all components magnetic jerk amplitudes per unit duration vary from a mean of $< \mathcal{A}/\mathcal{D}(max/4) >= 0.12$ nT/yr^3 (ϕ component in model $\mathcal{P}_1^0(t)$) up to $< \mathcal{A}/\mathcal{D}(max/4) >= 1.84$ nT/yr^3 (r component in model $\mathcal{P}_2^0(t)$). The $< \mathcal{A}/\mathcal{D}(max/2) >$ values are ~ 40 % larger than the $< \mathcal{A}/\mathcal{D}(max/4) >$ values, but the relative statistics is quite similar for both thresholds and for both steady and time-dependent models. For example, the ratio between largest to smallest is roughly the same for both thresholds (Tables 1 and 2).

The results for the jerk density in Table 2 are sensible. Given a jerk re-occurrence time of roughly half the assumed period of the time-dependent amplitude $T/2 = 25$ years, the order $\sim 1\%$ values of jerk density in Table 2 corresponds to about one quarter of the Earth's surface exhibiting a jerk once in 25 years. Based on the jerk density $< \rho(max/4) >$ in the time-dependent models for all components, the smallest densities are in $\mathcal{P}_2^0(t)$ (r component) and the largest in $\mathcal{T}_1^{1c}(t)$ (ϕ component).

Table 1: Jerk amplitude per unit duration in nT/yr^3 and normalized jerk density **in %** for the synthetic steady flow models. For both quantities the mean for values greater than one fourth/half of the maximum (e.g. $< \mathcal{A}/\mathcal{D}(max/4) >$ and $< \mathcal{A}/\mathcal{D}(max/2) >$, respectively) are given. For the jerk amplitude per duration the maximum values $\mathcal{A}/\mathcal{D}(max)$ are also given. **The first three rows are test cases using the $\mathcal{T}_1^0$ flow. In the first row a longer run of 100 years was used. In the second row the run was initialized with a dipole field. In the third row a lower $Rm = 500$ (i.e. a larger magnetic diffusivity) was tested. In all other rows simulations were run for 60 years, with an initial field model expanded to spherical harmonic degree and order $\ell_{max} = 14$ and with $Rm = 1000$.**

Model	component	$\mathcal{A}/\mathcal{D}$ (max)	$< \mathcal{A}/\mathcal{D}(max/4) >$	$< \mathcal{A}/\mathcal{D}(max/2) >$	$< \rho(max/4) >$	$< \rho(max/2) >$
$\mathcal{T}_1^0$ (100 yrs)	B_r	0.052	0.026	0.033	0.290	0.147
	B_θ	0.017	0.007	0.010	0.317	0.078
	B_ϕ	0.042	0.021	0.028	0.190	0.090
$\mathcal{T}_1^0$ (ℓ_{max}=1)	B_r	0.002	0.001	0.001	0.143	0.127
	B_θ	0.001	0.001	0.001	0.110	0.070
	B_ϕ	0.001	0.001	0.001	0.148	0.148
$\mathcal{T}_1^0$ (Rm=500)	B_r	0.052	0.026	0.034	0.279	0.148
	B_θ	0.015	0.007	0.010	0.332	0.096
	B_ϕ	0.042	0.021	0.028	0.315	0.148
$\mathcal{T}_1^0$	B_r	0.052	0.026	0.034	0.279	0.147
	B_θ	0.015	0.007	0.010	0.333	0.095
	B_ϕ	0.042	0.021	0.028	0.317	0.150
$\mathcal{T}_1^1$	B_r	0.094	0.056	0.067	0.213	0.103
	B_θ	0.075	0.037	0.050	0.228	0.086
	B_ϕ	0.067	0.030	0.040	0.163	0.033
$\mathcal{T}_2^0$	B_r	0.096	0.050	0.062	0.268	0.143
	B_θ	0.038	0.017	0.024	0.358	0.074
	B_ϕ	0.085	0.041	0.055	0.266	0.104
$\mathcal{T}_2^1$	B_r	0.140	0.082	0.102	0.179	0.071
	B_θ	0.117	0.051	0.081	0.147	0.038
	B_ϕ	0.098	0.037	0.06	0.161	0.014
$\mathcal{T}_3^0$	B_r.	0.159	0.082	0.105	0.255	0.128
	B_θ	0.070	0.030	0.045	0.335	0.050
	B_ϕ	0.143	0.061	0.095	0.250	0.054
$\mathcal{T}_5^4$	B_r	0.130	0.055	0.078	0.271	0.068
	B_θ	0.063	0.029	0.040	0.353	0.133
	B_ϕ	0.047	0.021	0.030	0.390	0.115
$\mathcal{P}_1^0$	B_r	0.132	0.073	0.093	0.220	0.121
	B_θ	0.141	0.059	0.100	0.239	0.062
	B_ϕ	0.029	0.013	0.017	0.285	0.106
$\mathcal{P}_2^0$	B_r	0.116	0.060	0.082	0.279	0.098
	B_θ	0.092	0.048	0.062	0.232	0.136
	B_ϕ	0.042	0.018	0.025	0.378	0.116
$\mathcal{P}_2^{2s}$	B_r	0.095	0.041	0.061	0.351	0.103
	B_θ	0.035	0.015	0.021	0.171	0.047
	B_ϕ	0.091	0.038	0.059	0.334	0.065
$\mathcal{P}_2^{2c}$	B_r	0.077	0.034	0.048	0.386	0.108
	B_θ	0.038	0.015	0.023	0.224	0.036
	B_ϕ	0.062	0.029	0.041	0.413	0.175
Mean	B_r	0.109	0.056	0.073	0.270	0.109
	B_θ	0.068	0.031	0.046	0.262	0.076
	B_ϕ	0.071	0.031	0.045	0.296	0.093

Table 2: As in Table 1 for the time-dependent models.

Model	component	$\mathcal{A}/\mathcal{D}$ (max)	$<\mathcal{A}/\mathcal{D}(max/4)>$	$<\mathcal{A}/\mathcal{D}(max/2)>$	$<\rho(max/4)>$	$<\rho(max/2)>$
$\mathcal{T}_1^0$ (100 yrs)	B_r	0.665	0.290	0.437	1.942	0.523
	B_θ	0.301	0.135	0.193	1.983	0.505
	B_ϕ	0.419	0.200	0.275	2,030	0.765
$\mathcal{T}_1^0$ (ℓ_{max}=1)	B_r	0.224	0.127	0.161	2.685	1.686
	B_θ	0.112	0.063	0.080	1.791	0.807
	B_ϕ	0.112	0.078	0.089	3.037	2.333
$\mathcal{T}_1^0$ (Rm=500)	B_r	0.664	0.290	0.436	1.943	0.523
	B_θ	0.301	0.134	0.193	1.983	0.506
	B_ϕ	0.419	0.200	0.275	2.032	0.766
$\mathcal{T}_1^0(t)$	B_r	0.665	0.290	0.437	1.942	0.523
	B_θ	0.301	0.135	0.193	1.983	0.505
	B_ϕ	0.419	0.200	0.275	2.030	0.765
$\mathcal{T}_1^1(t)$	B_r	1.992	0.902	1.314	1.674	0.576
	B_θ	0.933	0.446	0.606	2.019	0.831
	B_ϕ	0.720	0.386	0.486	2.724	1.446
$\mathcal{T}_2^0(t)$	B_r	1.145	0.483	0.752	1.368	0.326
	B_θ	0.592	0.251	0.411	1.045	0.106
	B_ϕ	0.698	0.315	0.443	1.786	0.505
$\mathcal{T}_2^1(t)$	B_r	0.832	0.379	0.520	1.790	0.625
	B_θ	0.547	0.229	0.332	1.629	0.289
	B_ϕ	0.509	0.211	0.316	1.958	0.438
$\mathcal{T}_3^0(t)$	B_r	1.292	0.523	0.794	1.259	0.263
	B_θ	0.663	0.285	0.449	1.084	0.144
	B_ϕ	0.727	0.333	0.459	1.600	0.398
$\mathcal{T}_5^4(t)$	B_r	0.796	0.344	0.513	1.265	0.349
	B_θ	0.624	0.255	0.405	0.899	0.232
	B_ϕ	0.339	0.157	0.218	1.925	0.714
$\mathcal{P}_1^0(t)$	B_r	1.577	0.824	1.070	2.465	0.912
	B_θ	1.204	0.578	0.761	2.652	1.157
	B_ϕ	0.254	0.120	0.165	2.360	0.868
$\mathcal{P}_2^0(t)$	B_r	3.413	1.836	2.325	0.656	0.224
	B_θ	1.518	0.783	1.039	2.057	0.927
	B_ϕ	0.475	0.180	0.303	1.402	0.173
$\mathcal{P}_2^{2s}(t)$	B_r	1.053	0.520	0.685	1.841	0.851
	B_θ	0.628	0.280	0.397	1.942	0.673
	B_ϕ	0.802	0.346	0.526	1.651	0.454
$\mathcal{P}_2^{2c}(t)$	B_r	1.045	0.495	0.672	1.883	0.805
	B_θ	0.586	0.269	0.377	1.883	0.722
	B_ϕ	0.663	0.323	0.444	1.850	0.806
Mean	B_r	1.381	0.660	0.908	1.614	0.545
	B_θ	0.760	0.351	0.497	1.719	0.559
	B_ϕ	0.561	0.257	0.364	1.929	0.657

To get some insight into the relation between the flow and the jerk morphology, we calculated the radial magnetic field B_r, its SV, SA and the third time derivative of the field at both the CMB and at the Earth's surface, for the steady **and for the time-dependent $\mathcal{T}_1^0$ and $\mathcal{T}_1^0(t)$ flows respectively,** in a snapshot (Figs. 4 and 5). At the CMB the resulting SV, SA and the third derivative are most intense at lower latitudes (Figs. 4b-d and 5b-d) where the zonal flow is larger. Higher order time derivatives yield smaller scales and a sectorial dominance **in the steady model** (Fig. 4d). By definition, intense third time derivative at the Earth's surface corresponds to regions of jerks. Because jerks are surface features, large-scales are expected to dominate. On the other hand, higher order time derivatives give smaller dominant length scales **in the steady model**, in this case sectorial dominance. Indeed, **in the steady model** at the Earth's surface, the SV is dominated by Y_1^1 (Fig. 4f), the SA by Y_3^3 (Fig. 4g) and the third

time derivative by Y_6^6 Fig. 4h), with increasingly clearer emergence of sectorial dominance at the higher order time derivatives. In this particular case the field as well as its time derivatives simply drift to the east, hence jerks are also expected to drift eastward with time, as shown in Fig. 6.

In the time-dependent model the patterns are practically identical for the SV, SA and third time derivative, which are all dominated by Y_1^1 (Fig. 5). The reason for this similarity is the dominance of the flow acceleration term in the SA equation (3), which can be demonstrated analytically. In case $\mathcal{T}_1^0(t)$ the flow is simply

$$\mathbf{u_h} = \frac{\alpha(t)}{R_c} \sin\theta \hat{\phi} \tag{19}$$

Substituting (19) into (1) and neglecting the diffusion term gives

$$\dot{B}_r = -\frac{\alpha(t)}{R_c^2} \frac{\partial B_r}{\partial \phi} \tag{20}$$

Substituting (19) into (3) and further neglecting the terms that involve the interaction of the flow and the SV gives

$$\ddot{B}_r \simeq -\frac{\dot{\alpha}(t)}{R_c^2} \frac{\partial B_r}{\partial \phi} \tag{21}$$

and likewise

$$\dddot{B}_r \simeq -\frac{\ddot{\alpha}(t)}{R_c^2} \frac{\partial B_r}{\partial \phi} \tag{22}$$

Equations (20-22) explain the identical patterns of SV, SA and the third time derivative of B_r in the case of the $\mathcal{T}_1^0(t)$ flow. Furthermore, this analytical solution confirms that indeed the flow acceleration terms dominate the SA in our solutions.

By definition, magnetic jerks in the radial component are detected in intense regions of third time derivative of the radial field (compare Figs. 4h and 5h with Figs. 6a and Fig. 7a, respectively). In the steady model the pattern of north-south strips characterizes the sectorial harmonics. In the time-dependent model jerks reside at regions of large azimuthal field gradients (22). Note the difference between the scales in Figs. 4h and 5h, demonstrating jerks more than an order of magnitude stronger in the time-dependent model. The results for the θ and ϕ components are more complicated to interpret since the maximum contribution of the radial field at the CMB to the horizontal components of the field at the surface is at about 23° angular distance from a measurement site rather than right below it (e.g. Gubbins, 2004). Nevertheless the sectorial pattern is evident (though shifted) in the ϕ component as well **(Figs. 6c and 7c)**, while the θ component is about **2-4** times weaker **than the radial component (Figs. 6b and 7b)**.

Other toroidal zonal steady flow models ($\mathcal{T}_2^0$ and $\mathcal{T}_3^0$) also result in sectorial magnetic jerk patterns, again more intense in the r component (Table 1). **For** the $\mathcal{T}_1^0$ **flow** jerks are weaker at high latitudes (Fig. 6) where the flow is weaker. Almost all north-south jerk strips in this

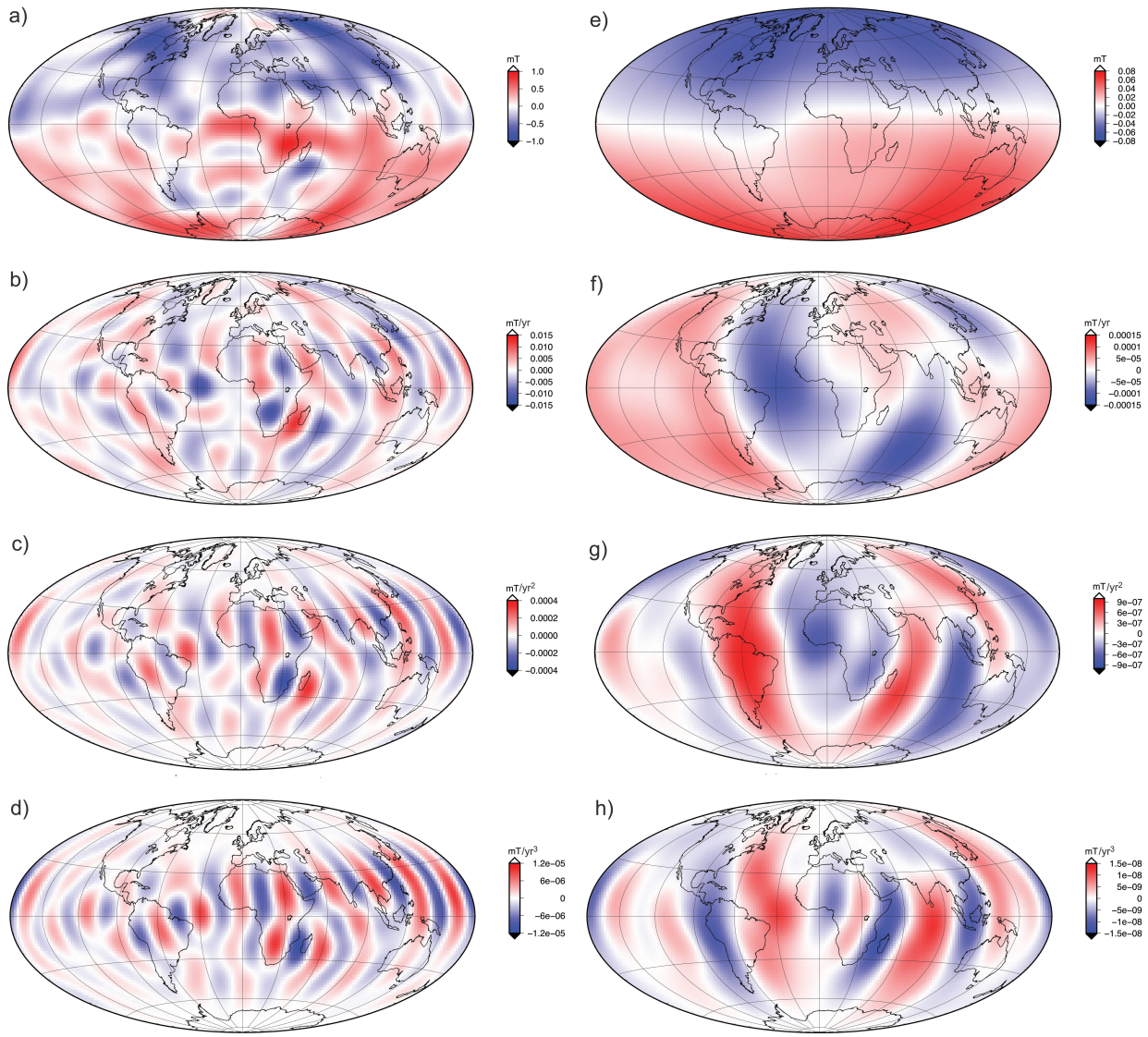

Figure 4: Radial magnetic field (a,e), secular variation (b,f), secular acceleration (c,g) and third time derivative (d,h) at the CMB and at the Earth's surface, respectively, calculated for a snapshot 30 years after the simulation started with the synthetic steady toroidal flow model $\mathcal{T}_1^0$.

model extend across the equator. In $\mathcal{T}_2^0$ (not shown) such strips extend to higher latitudes and most of them do not reach the equator where the flow vanishes in this case. Jerks in $\mathcal{T}_2^0$ drift to the east in the Northern Hemisphere and to the west in the Southern Hemisphere. The absence of any shear (in this case north-south derivative of the azimuthal angular momentum) in model $\mathcal{T}_1^0$ gives north-south strips with approximately the same thickness for different jerk

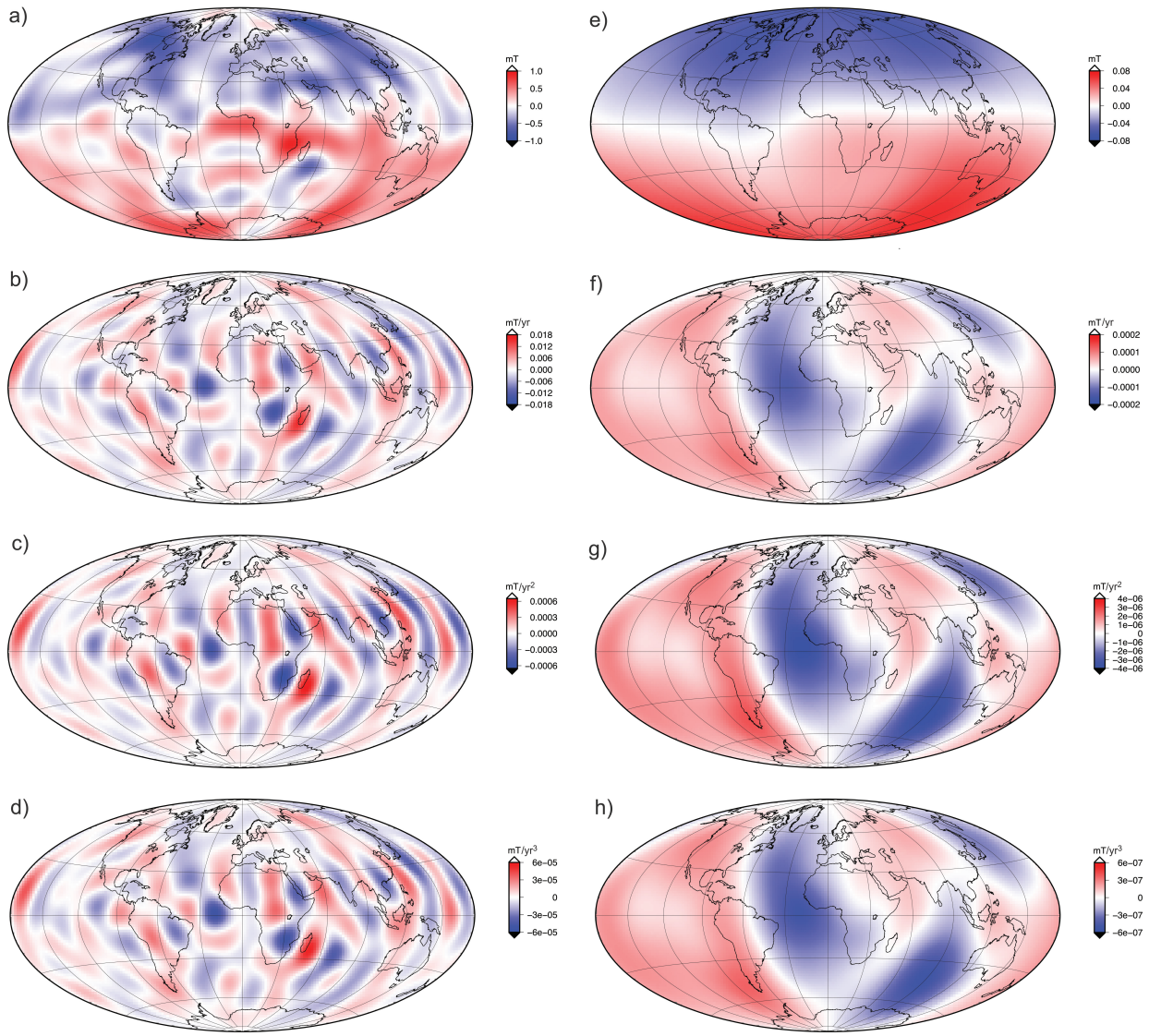

Figure 5: As in Fig. 4 but with the synthetic time-dependent toroidal flow model $\mathcal{T}_1^0(t)$.

occurrence times, which means same surface area with jerks for different epochs (Fig. 6).

The results of some time-dependent models are given in Figs. 7 and 10-12. Our visualization scheme relies on colors for time and symbol size for jerk amplitude per duration time. Fig. 8 demonstrates the scheme using a zoom into **results obtained with** model $\mathcal{T}_1^0(t)$. In this case over a relatively small region distinctive values of $\mathcal{A}/\mathcal{D}$ are seen, from weak below 0.066 nt/yr^3 south of the tip of Africa to more than 4.5 times stronger values of above 0.304 nt/yr^3 west of Africa.

Our visualization scheme does not distinguish between a single delayed jerk vs. multiple isolated jerk events. Fig. 9 shows that in SV time series of jerks at neighboring locations the signs are correlated. Thus, in our maps of jerk spatio-temporal distributions (Figs. 7-8 and 10-12), different colors in nearby regions correspond to delayed jerks rather than multiple jerk events.

The time-dependent model $\mathcal{T}_1^0(t)$ (Fig. 7) gives distinctive results compared to its corresponding steady flow model (Fig. 6). Apart from the $\sim$ 10-20 times larger jerk **amplitude per unit duration time** in the time-dependent model (Tables 1-2), the main difference is that the steady model presents a localized pattern of jerk occurrences while the time-dependent model shows a more global pattern. In the steady case north-south strips of uniform thickness appear whereas in the time-dependent case there are non-uniform strip thicknesses (non-linearity), which means different areas with jerks for different epochs. In Fig. 7 there are clearly more jerks in a given epoch (see mostly yellow between 1990 and 1995). In this simple $\mathcal{T}_1^0$ flow pattern the interpretation of the direction of propagation of jerks is straightforward. The eastward drift in the steady case (Fig. 6) reflects the flow direction, whereas the westward drift in the time-dependent case (Fig. 7) reflects the acceleration direction. In addition, the uniform strip thickness in Fig. 6 reflects the constant angular velocity in the steady $\mathcal{T}_1^0$ flow, while the non-uniform strip thickness in Fig. 7 reflects the time-dependent flow amplitude in (6).

The time-dependent $\mathcal{T}_3^0(t)$ model (Fig. 10) results in a more complex configuration of magnetic jerks than in the $\mathcal{T}_1^0(t)$ model (Fig. 7). In all three components the morphology of early/late jerks are more irregular in the $\mathcal{T}_3^0(t)$ model, $\mathcal{A}/\mathcal{D}$ is larger and presents a greater spatial variability (see size of circles) and magnetic jerk densities are smaller. Similarly to the $\mathcal{T}_1^0(t)$ model, there are more jerks in specific periods (yellow circles) when the acceleration is larger (Figs. 7 and 10) .

Unlike the elongated strips of jerk occurrences found in our larger scale models, our smallest scale time-dependent flow model $\mathcal{T}_5^{4c}(t)$ (Fig. 11) yields highly non-linear jerks occurrence times with concentrations of jerks in a given epoch and region. For example, in Fig. 11b (θ component) Africa is strongly characterized by late jerk occurrence times, and in the r component (Fig. 11a) in the North Pacific a circular region with jerks arriving at approximately the same time (yellow) in the center and at later times in the margins (red) is observed.

Four poloidal flow models were considered. Based on $< \rho(max/4) >$, the time-dependent model $\mathcal{P}_1^0(t)$ gives the largest jerk densities for all three components (Table 2). This model is characterized by east-west strips (**not shown**), especially in the r and θ components, while in the ϕ component jerk morphology is more complex. The propagation of magnetic jerks in $\mathcal{P}_1^0(t)$ does not follow the flow from the south to the north, as is the case in the steady flow model (not shown). Instead, the east-west strips propagate in the (northern or southern) direction of the acceleration with broadest regions when the acceleration is fastest as in $\mathcal{T}_1^0(t)$ **and** $\mathcal{T}_3^0(t)$ **(Figs. 7 and 10)**.

The $\mathcal{P}_2^{2s}(t)$ and $\mathcal{P}_2^{2c}(t)$ time-dependent models give expected order 2 signatures in the jerk occurrences especially in the r and θ components (e.g. Fig 12), with mostly phase differences

between the two models. The statistics of the two models is therefore similar (Tables 1-2) as expected. In both cases large-scale accelerating upwelling/downwelling structures yield circular jerk occurrences patterns (Fig. 12).

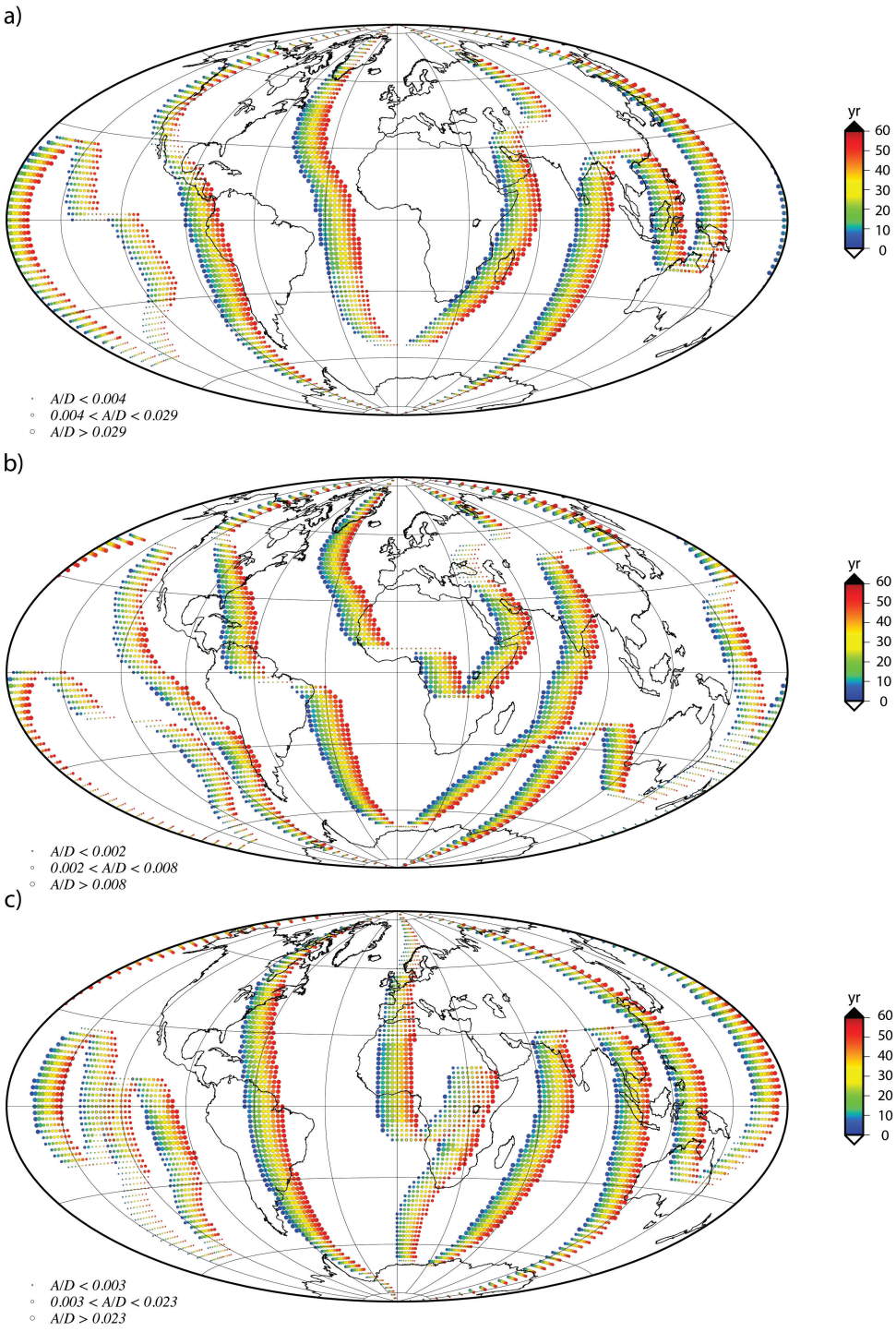

Figure 6: Magnetic jerk occurrence times (color) and **absolute** amplitudes per unit duration (sizes of circles in nT/yr^3, see legend) for the synthetic steady toroidal flow model $\mathcal{T}_1^0$ in the r (top), θ (middle) and ϕ (bottom) components. Note that the scales differ among the components.

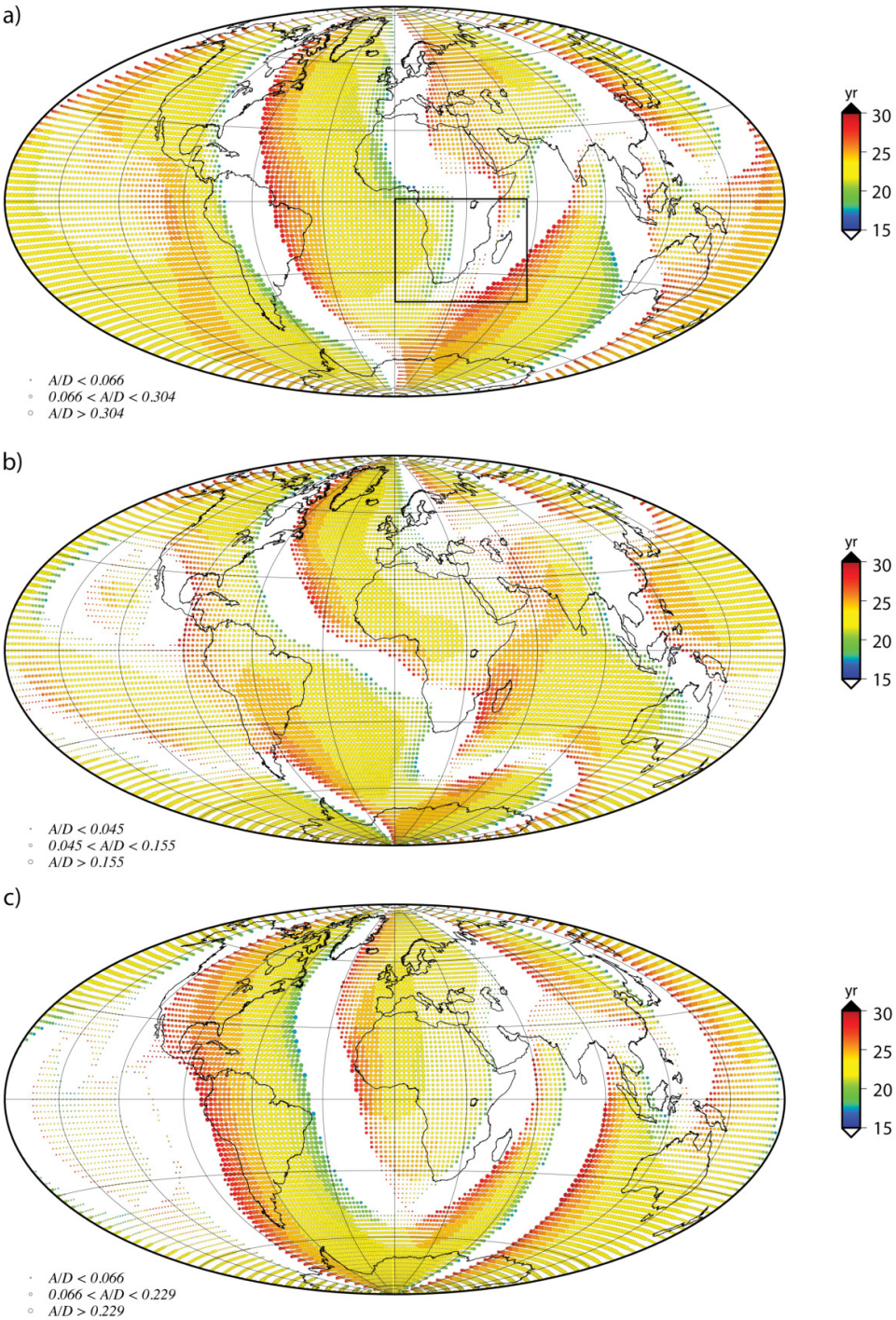

Figure 7: As in Fig. 6 for the synthetic time-dependent toroidal flow model $\mathcal{T}_1^0(t)$. In a few cases where two jerk events occur they are represented by diamonds **(see also Fig. 8)**. Note that the $\mathcal{A}/\mathcal{D}$ values here may slightly differ from those in Table 2 because the period here is shorter for better visualization.

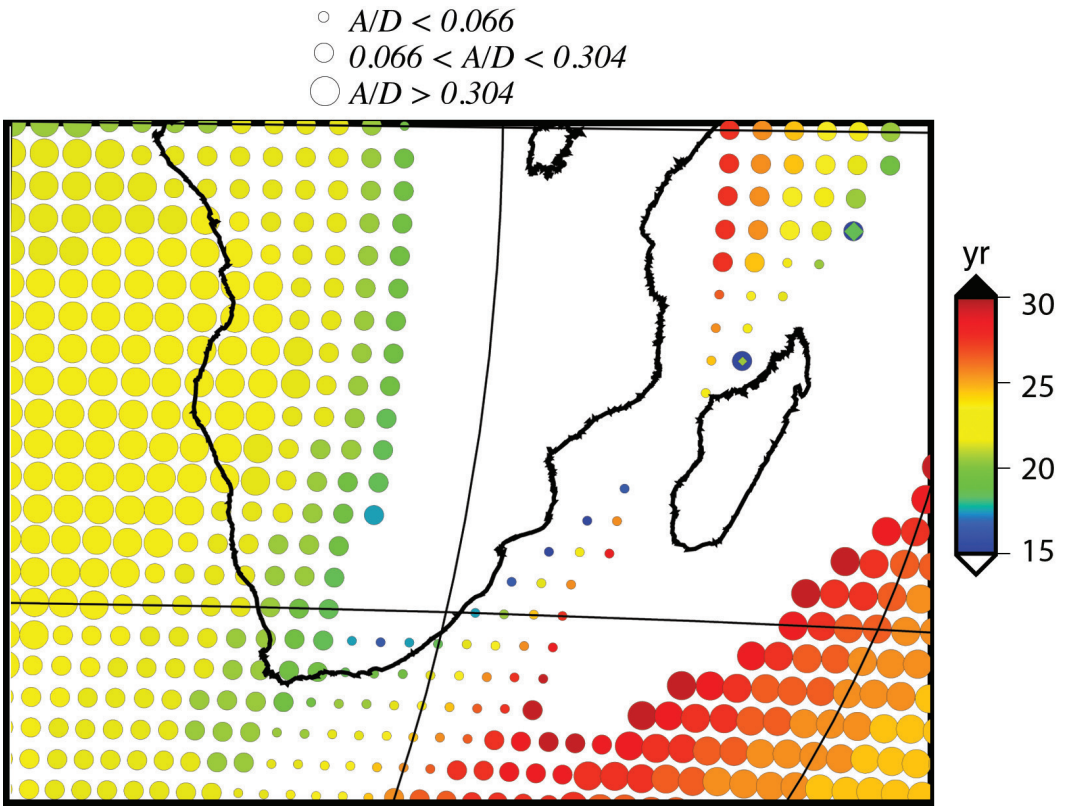

Figure 8: Zoom into the South Africa region in Fig. 7a to illustrate different sizes of the symbols that represent three ranges of **absolute** $\mathcal{A}/\mathcal{D}$ values (in units of nT/yr^3, see legend). The colors indicate the jerk occurrence times. **Note diamonds near Madagascar representing a second jerk event.**

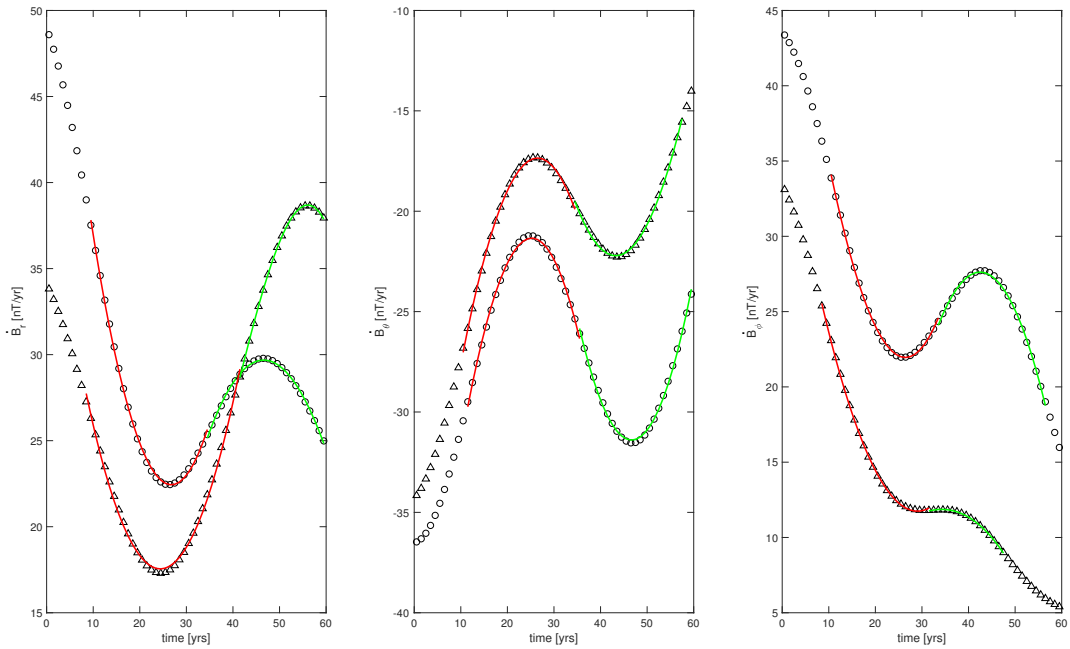

Figure 9: Secular variation time series for the synthetic time-dependent toroidal flow model $\mathcal{T}_1^0(t)$ in the r (left), θ (middle) and ϕ (right) components. Circles represent the SV at longitude $148°$**E** and triangles at longitude $138°$**E**, both at the equator. The red and green lines are the polynomial fits of the two jerk events.

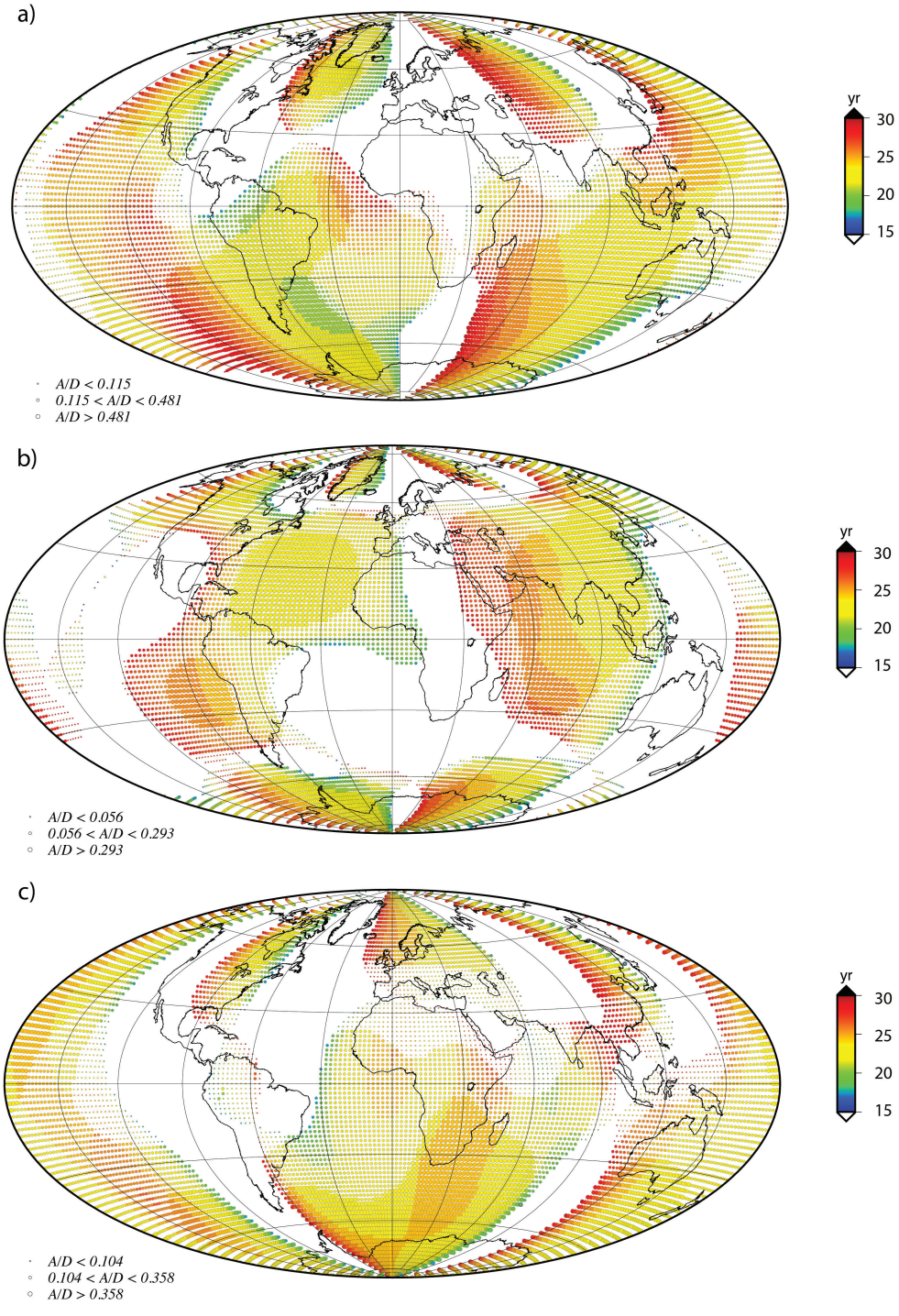

Figure 10: As in Fig. 7 for the synthetic toroidal flow model $\mathcal{T}_3^0(t)$.

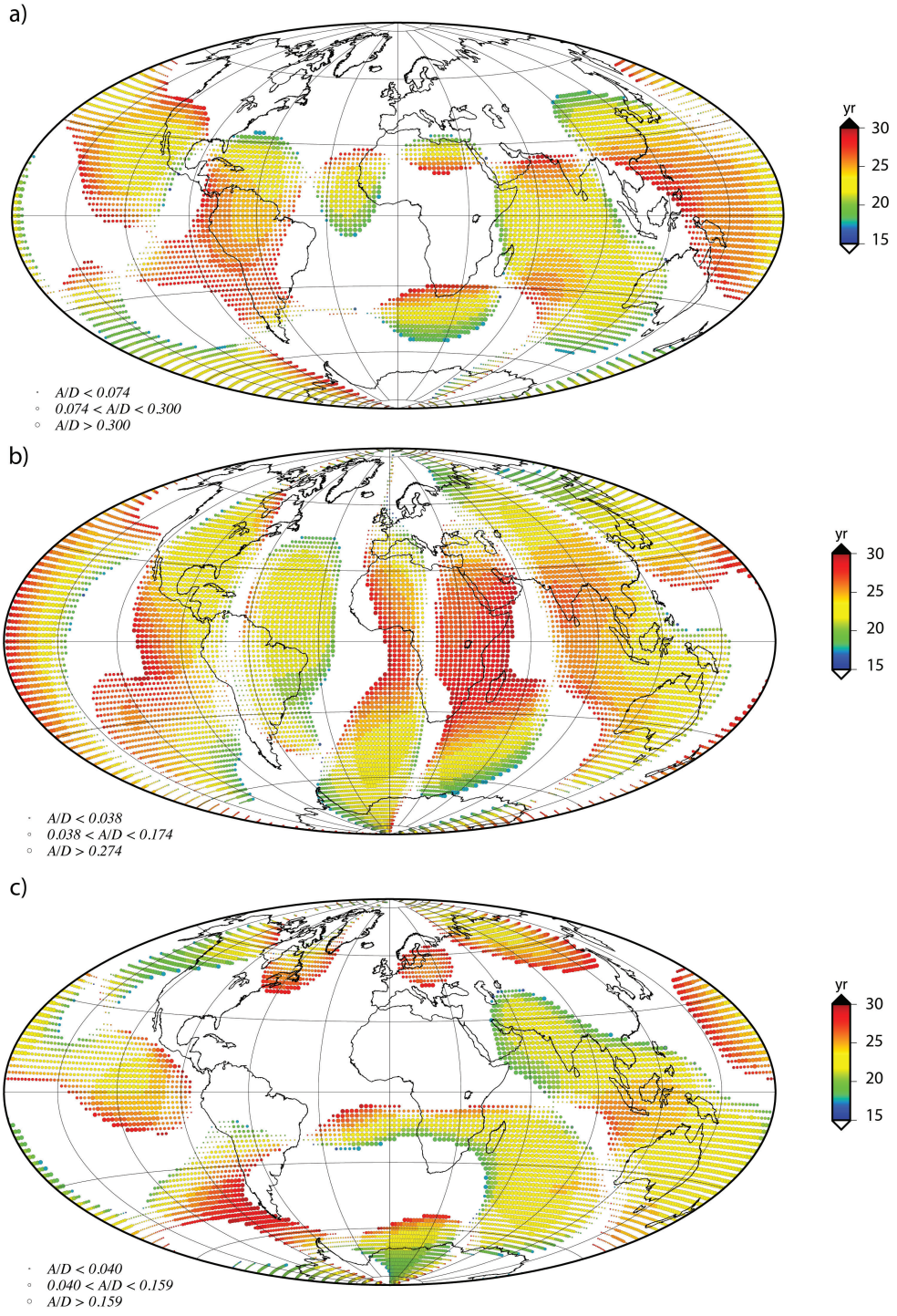

Figure 11: As in Fig. 7 for the synthetic toroidal flow model $\mathcal{T}_5^{4c}(t)$.

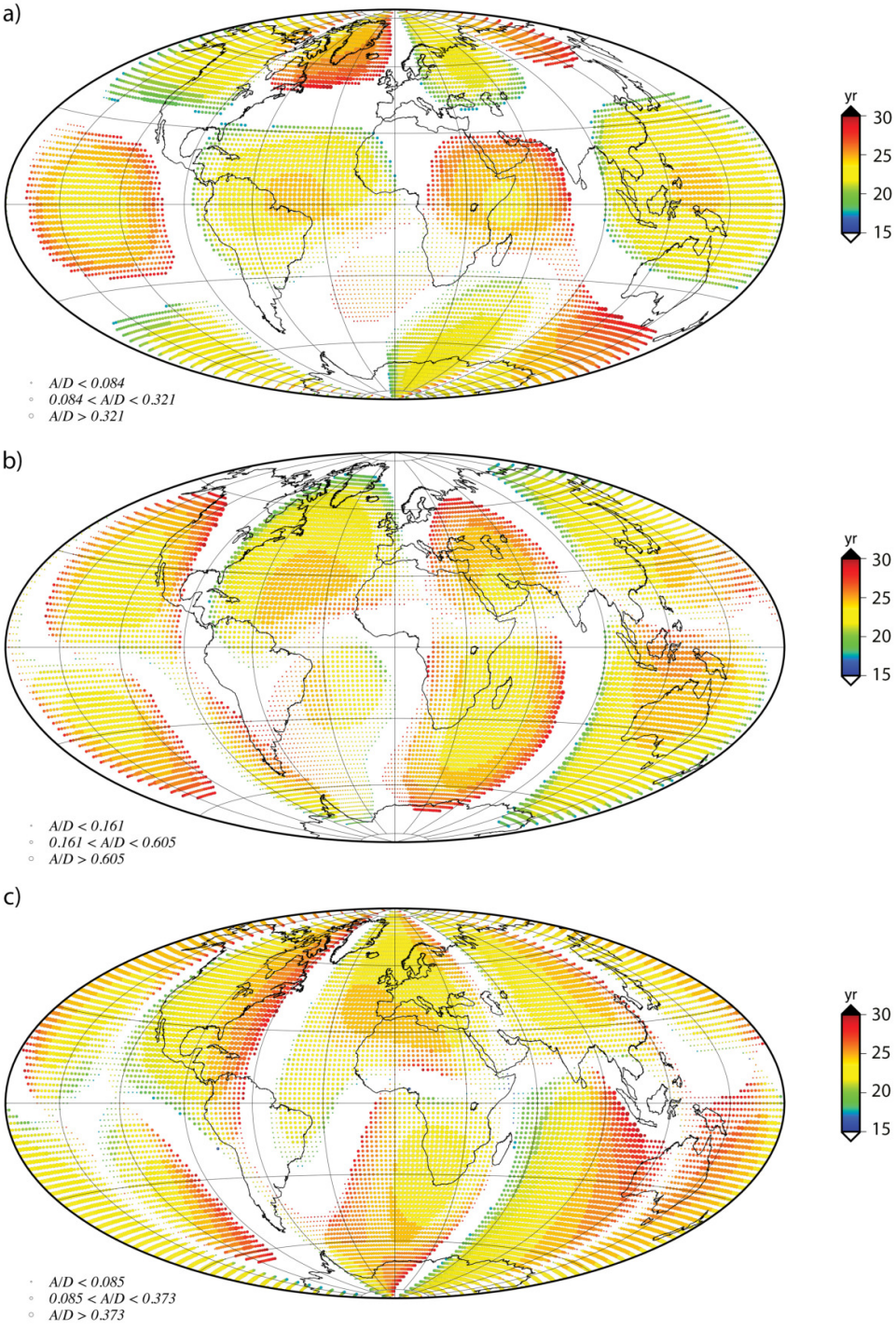

Figure 12: As in Fig. 7 for the synthetic poloidal flow model $\mathcal{P}_2^{2s}(t)$.

3.2 Geomagnetic jerks detected using observatory data

Here we present results of jerk detection and characterization in geomagnetic data **using the same method as for the synthetic jerks**. We sample ten observatories from various regions of the Earth to demonstrate the typical geomagnetic jerk amplitudes and spatio-temporal characteristics. Because our large-scale synthetic flows yield smooth SV time series and magnetic jerks which are better fitted by a third order polynomial than by two line-segments **(e.g. Pinheiro et al., 2011)**, we also applied the polynomial fit to the geomagnetic jerks. Thus first we compared the line-segments and polynomial fits in the geomagnetic jerks. Second we compared jerk amplitudes per duration time $\mathcal{A}/\mathcal{D}$ in our synthetic models and in geomagnetic data using the polynomial fit.

We selected ten magnetic observatories from different regions of Earth's surface: L'Aquila (AQU, Italy), Dourbes (DOU, Belgium), Fredericksburg (FRD, USA), Gnangara (GNA, Australia), Kakioka (KAK, Japan), Macquarie Island (MCQ, Australia), Meanook (MEA, Canada), Niemegk (NGK, Germany), Tromso (TRO, Norway) and Victoria (VIC, Canada). In some cases we were not able to detect jerks ("non-detected"- nd), essentially when the fits do not contain a change of sign of SA (see section 2.2). We applied the two fits **exclusively** to the Y (i.e. ϕ) component of the well-known 1969 and 1978 geomagnetic jerks **because it is considered as the least contaminated by the external field (e.g. Wardinski and Holme, 2011; Balasis et al., 2016; Cox et al., 2018). We monitored** jerk occurrence times, **amplitudes per unit duration time** and misfits (Tables 3 and 4 respectively).

Based on the two line-segments fit, the average absolute difference between jerk occurrence times in the two fits is 0.9 years in the 1969 jerk and 1.7 years in the 1978 jerk (Tables 3-4). **Pinheiro et al. (2011) calculated error bars on jerk occurrence times and amplitudes. For the ϕ component, they found a mean error of $\pm$ 0.95 years and $\pm$ 1.15 years for the occurrence times of the 1969 and 1978 jerks, respectively. Therefore, the difference between jerk occurrence times in the two methods (Tables 3-4) are within the associated errors.** In the 1969 jerk, the differences in t_0 between the two methods range from 0.2 years for the TRO observatory (Fig. 13) to 3.0 years for the VIC observatory (Table 3). In the 1978 jerk, these differences range from 0.9 years for the AQU observatory to 3.4 years for the TRO observatory (Fig. 14 and Table 4). In both methods, on average the 1969 jerk was stronger (larger $\mathcal{A}/\mathcal{D}$ and $\mathcal{A}$) than the 1978 jerk. The misfits are in general slightly larger in the polynomial fits than in the two line-segments fits, by about 5% (Tables 3-4). In the 1969 jerk, the observatories AQU, DOU and KAK have identical misfits in the two methods (Table 3).

In the **observed** geomagnetic jerks $\mathcal{A}/\mathcal{D}$ is about an order of magnitude larger than the $\mathcal{A}/\mathcal{D}(max)$ in the **synthetic** steady models (Tables 1-2). **Comparing the synthetic** time-dependent models (Table 2) and geomagnetic (Tables 3 and 4) jerks, the strongest synthetic jerk reaches a value of $\mathcal{A}/\mathcal{D}(max) \sim 3.4$ nT/yr^3 **in the radial component and** $\mathcal{A}/\mathcal{D}(max) \sim 0.8$ **nT/yr^3 in the ϕ component,** whereas the strongest geomagnetic jerk reaches $\mathcal{A}/\mathcal{D} \sim 2.8$ nT/yr^3. In the geomagnetic jerks the mean $\mathcal{A}/\mathcal{D}$ considering the two jerks (1969 and 1978)

is 1.1 nT/yr^3, which is smaller than the mean of the radial component of $\mathcal{A}/\mathcal{D}(max)$ in the time-dependent models ($\sim$ 1.4 nT/yr^3) **but larger than the mean of the ϕ component ($\sim$ 0.6 nT/yr^3)**. Overall the values of jerk amplitudes per duration time of the **synthetic** time-dependent models and **observed** geomagnetic jerks are of the same order of magnitude, i.e. these models are in good agreement with the observations.

Table 3: Characterization of the 1969 geomagnetic jerk (Y component) in ten magnetic observatories: L'Aquila (AQU), Dourbes (DOU), Fredericksburg (FRD), Gnangara (GNA), Kakioka (KAK), Macquarie Island (MCQ), Meanook (MEA), Niemegk (NGK), Tromso (TRO) and Victoria (VIC). Occurrence time is t_0 in years, amplitude is $\mathcal{A}$ in nT/yr^2, amplitude per unit duration is $\mathcal{A}/\mathcal{D}$ in nT/yr^3 and misfit is σ in nT/yr. The first values correspond to the two line-segment fit and the second to the third order polynomial fit. Non-detected jerks are denoted by "nd".

obs	t_0	$\mathcal{A}, \mathcal{A}/\mathcal{D}$	σ
AQU	1969.3, 1968.8	5.0, 1.1	1.5, 1,5
DOU	1969.3, 1968.6	6.3, 2.0	1.9, 1,9
FRD	nd, nd	nd, nd	nd, nd
GNA	1971.9, 1971.2	5.0, 0.8	1.7, 2.3
KAK	1969.4, 1968.8	2.9, 0.9	0.9, 0.9
MCQ	1971.0, 1971.7	4.7, 0.7	5.1, 5.3
MEA	1969.4, 1968.2	7.3, 2.8	3.2, 3.3
NGK	1969.4, 1969.0	6.7, 1.7	1.1, 1.3
TRO	1969.0, 1968.8	7.6, 2.2	2.3, 2.6
VIC	1971.5, 1968.5	5.9, 0.8	1.8, 1.9
Mean	1970.0, 1969.3	5.7, 1.4	2.2, 2.3

Table 4: As in Table 3 for the 1978 geomagnetic jerk. **Note that the three stations where jerks were not detected by one of the approaches were excluded from the calculation of the mean values.**

obs	t_0	$\mathcal{A}, \mathcal{A}/\mathcal{D}$	σ
AQU	1982.0, 1981.1	4.4, 0.9	3.3, 3.4
DOU	1978.4, 1980.1	4.3, 0.7	2.1, 2.0
FRD	1979.5, 1977.8	2.3, 0.5	1.1, 1.1
GNA	1981.4, nd	4.1, nd	3.2, nd
KAK	1978.0, nd	0.8, nd	1.3, nd
MCQ	nd, 1978.7	nd, 0.7	nd, 6.1
MEA	1982.7, 1981.7	5.6, 1.1	2.4, 2.6
NGK	1978.2, 1980.2	5.0, 0.7	1.4, 1.7
TRO	1978.0, 1981.4	3.7, 0.7	3.1, 3.2
VIC	1977.3, 1978.8	7.3, 1.2	2.1, 1.9
Mean	1979.4, 1980.2	4.7, 0.8	2.2, 2.3

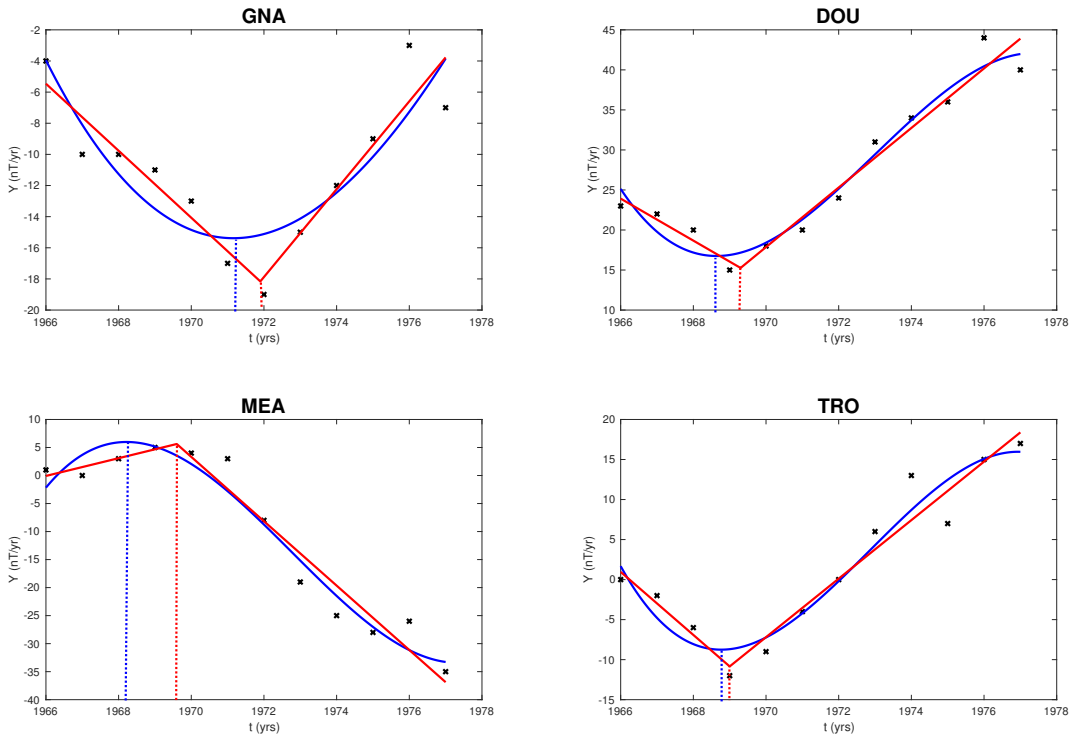

Figure 13: Geomagnetic data (black crosses) of four surface observatories during the 1969 geomagnetic jerk. The observatories are Niemegk (NGK), Gnangara (GNA), Hermanus (HER) and Fuquene (FUQ). The respective two line-segments fits (red) and third order polynomial fits (blue) are given. **Red and blue vertical dotted lines denote the intersections** of the two line-segments and the extreme points of the polynomial curves **respectively, indicating the** fitted occurrence times of the two methods respectively.

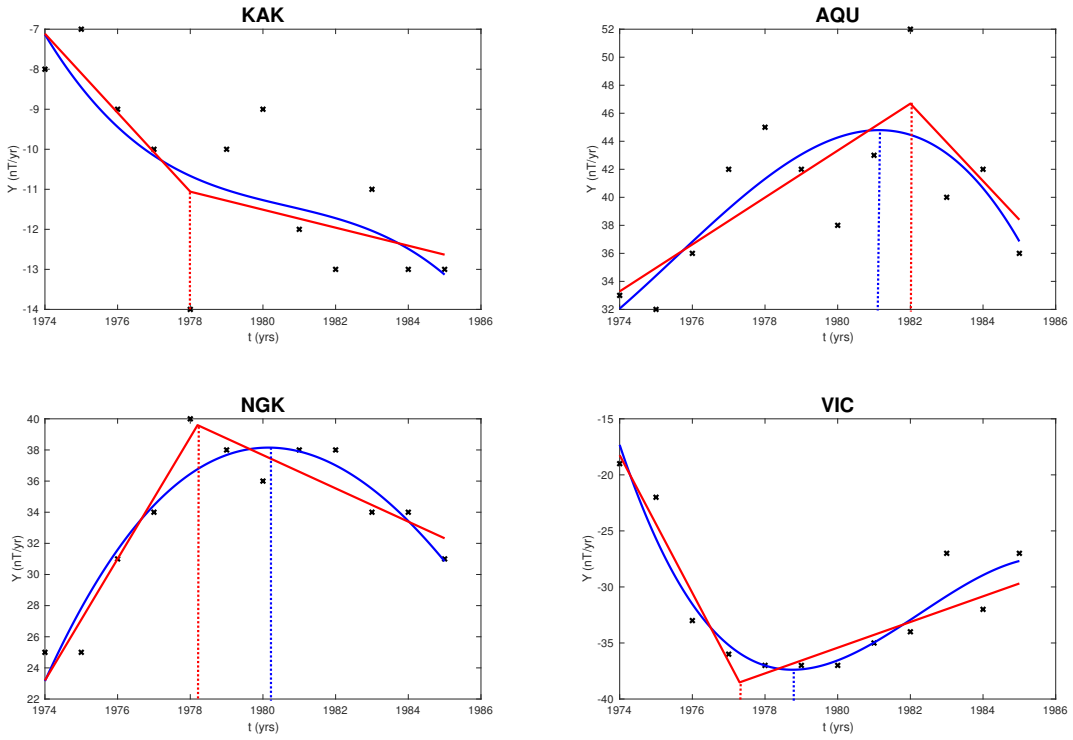

Figure 14: As in Fig. 13 for the 1978 geomagnetic jerk.

4 Discussion

Most attempts to identify the dynamical origin of geomagnetic jerks relied on core flow models from geomagnetic SV inversions, **(e.g. Bloxham et al., 2002; Silva and Hulot, 2012; Beggan and Whaler, 2018)**. **These SV inverted models are clearly more geophysically meaningful than our synthetic flows, because the former are constrained by the geomagnetic field for the whole period. However, these** inversions have some limitations, most notably the non-uniqueness of the solutions typically requires physical assumptions on the flows (e.g. Holme, 2015). Alternatively, instead of trying to fit the flows to explain observed jerks, we adopted a more fundamental approach to reveal the role of various flow components in generating jerks and their spatio-temporal features. We forward solved the induction equation using an initial magnetic field as in Cox et al. (2016). However, for a broader and more fundamental exploration of kinematic scenarios, instead of considering a torsional oscillation model (Cox et al., 2016), we explored a suite of generic single harmonic flow models. **In addition, Cox et al. (2016) let a small perturbation field evolve in time by the torsional waves while keeping a background large-scale field fixed, whereas in our case the entire field evolves with time due to the flow in a consistent way.**

The recent work by Aubert (2018) provides a breakthrough in the study of the dynamical origin of geomagnetic jerks. His dynamo model is in an asymptotic parametric regime where damping is weak enough so that rapid phenomena like jerks may emerge. **Aubert (2018) highlighted the importance of the separation between the typical SA time and the advection time. In his dynamo model, quasi-geostrophic Alfvén waves advect flow acceleration to the outer boundary of the shell, resulting in SA pulses.** However, the SA pulses in his model are very frequent and strongly localized at the equatorial region, similar to recent satellite era jerks, but rather different from the more isolated in time and more global historical jerks of e.g. 1969 and 1978.

The classical definition of geomagnetic jerks is a "V-shape" in the SV. These abrupt changes of trend in the SV have been fitted by different methods such as piecewise straight-lines (Mouël et al., 1982; Chambodut and Mandea, 2005; Olsen et al., 2006; Pinheiro et al., 2011; Brown et al., 2013) and wavelet analysis (Alexandrescu et al., 1996; Michelis and Tozzi, 2005). The fitting of two line-segments considers that jerks are a "V-shape" in the SV, consequently a step-function in the second time-derivative and an impulse in the third time-derivative. In the wavelet transform technique jerks are assumed to be singularities at the CMB, with the singularity being defined as a discontinuity in an x derivative of the signal, where x is its regularity. In the case of the two line-segments fitting the jerk is characterized by $x = 2$ but in the wavelet analysis $x = 1.5$ (Alexandrescu et al., 1996), i.e. an even sharper signature of a jerk. In constrast, this classical definition of jerks **was questioned by e.g. Demetrescu and Dobrica (2014) who pointed** that abrupt changes in the SV may be caused by the external field**, although most studies favored an internal origin for jerks (e.g. Nagao et al., 2003; Brown et al., 2013).** Cox et al. (2016) also favored smoothly varying SV over abrupt changes. Overall, jerks may be somewhat smoother than what is often considered.

There are three main differences between this work and previous attempts to explain geomagnetic jerk features. First, we **proposed** that jerks may be caused by simple single harmonic flows with a steady pattern and a mildly time-dependent amplitude without resorting to changes of direction. Therefore, jerks are not necessarily caused by drastically time-varying flows. Second, we calculated jerk occurrence times and **amplitudes per unit duration time** using a third order polynomial fit, by invoking a new formalism of jerk amplitude per unit duration time $\mathcal{A}/\mathcal{D}$. Finally, we designed a new visualization scheme for occurrence times and amplitudes (Figs. 7-12).

Applying the polynomial fit instead of the two line-segments gives different occurrences times (Figs. 13-14), which results in different patterns of jerk differential delays, hence may provide new constraints on mantle electrical conductivity modeling (Pinheiro and Jackson, 2008). Our visualization scheme provides a concise spatio-temporal image of jerk occurrences and amplitudes per unit duration time. The polynomial fit is most applicable if the jerks are somewhat smooth (Cox et al., 2016) or if some finite duration time exists (Nagao et al., 2003), whereas this approach is limited if the jerks are abrupt. The visualization scheme is applicable for periods shorter than the jerk re-occurrence period whereas high frequency re-occurring jerks is more challenging to visualize.

Due to the large Rm estimates for Earth's core (e.g. Roberts and Scott, 1965), magnetic diffusion is often considered negligible on short timescales. This assumption is possibly wrong. Expansion and intensification of reversed flux patches on the CMB suggests substantial magnetic diffusion contributions to the SV (e.g. Gubbins, 1987; Olson and Amit, 2006). Unfortunately, such flux expulsion (Bloxham, 1986) is not accessible from observations because the field inside the core is generally unknown. The accessible part of the diffusion, i.e. tangential diffusion (last term in Eq. 1), which can be mapped from geomagnetic field models, is indeed negligible (Amit and Christensen, 2008). Here we used this tangential diffusion term for numerical stability purposes. This term has no impact on the jerk generation. Indeed, same flows with two distinctive Rm values (500 and 1000) give practically identical statistics (Tables 1-2).

Our results provide insights to the relation between core kinematics and jerk occurrence patterns. We first calculated SV time series induced by steady flow models as a reference to the time dependent models. The objective was to test whether a mild time-dependence is capable of generating Earth-like jerk amplitudes and recover their spatio-temporal characteristics. We obtained some interesting insights from the simpler steady flow models: when the flow is azimuthal north-south strips of SA change of sign follow the direction of the flow (see blue to red to the east in Fig. 6), whereas for meridional flows east-west strips appear **(see Fig. 12)**. Convergence/divergence zones interacting with intense radial field often produce circular patterns of occurrence times in the steady and time-dependent flow models (e.g. Fig. 12a). Similar circular patterns were detected in geomagnetic data for the 1978 and 2007 jerks (Chambodut and Mandea, 2005; Chulliat et al., 2010). Such morphologies may allow to distinguish regions of jerks induced by magnetic field stretching (circles) or by advection (elongated strips).

In general, non-simultaneous jerks may arise due to a combination of the mantle filtering (e.g. Alexandrescu et al., 1999; Nagao et al., 2003) and dynamical processes in the core. Pinheiro and Jackson (2008) argued that in order to recover the observed differential delay times of ~ 3 yr, unrealistically high mantle electrical conductivity models are required. Our synthetic models demonstrate that the non-simultaneous behavior of magnetic jerks manifested by their early/late occurrences may arise due to dynamical processes in the core, **without the need to invoke mantle electrical conductivity filtering effects (e.g. Pinheiro and Jackson, 2008)**. Moreover, only a mild time variation on the flow amplitudes is required. The non-simultaneous jerk behaviour obtained in our models are in general agreement with the delay times observed in geomagnetic jerks. Within the 15-years period displayed in Figs. 7-12, most of the jerks occur between 1990-1995 (green to orange) especially around 1993 (yellow). Such 5-years interval of differential delays is in good agreement with observed geomagnetic jerks (Pinheiro and Jackson, 2008). **However, comparing our results with a complete spatial coverage to the historical jerks recorded using a sparse network of surface observatories is obviously non-satisfactory. Here satellite data may provide a more adequate constraint to our models.**

The resulting non-simultaneous jerks presented non-linear patterns in the time-dependent models. Shear flow as well as flow acceleration lead to a non-uniform pattern of jerk strip thicknesses, i.e. preferential times when magnetic jerks occur. In some cases this non-linearity is more prominent e.g. as in model $\mathcal{T}_5^{4c}(t)$ (Fig. 11) than in others e.g. as in $\mathcal{T}_1^0(t)$ (Fig. 7). In geomagnetic jerks the non-linearity is evident in wider areas of certain occurrence times (e.g. Alexandrescu et al., 1996; De Michelis et al., 1998; Mandea et al., 2010; Pinheiro et al., 2011).

The spatial variability of occurrences reflects the local/global patterns of jerks. A geomagnetic jerk is classified as global when detected in most of the available magnetic observatories; that is the case for example for the 1969, 1978 and 1991 events (Alexandrescu et al., 1996; Nagao et al., 2002; Chambodut and Mandea, 2005; Pinheiro et al., 2011; Brown et al., 2013). However, the non-uniform geographical distribution of observatories is a clear limitation for such interpretations. For example, if jerk strips as in our models fortuitously coincide with most observatories, the resulting jerks might be erroneously characterized as global. If a jerk is detected at only part of the existing surface observatories it may be considered as non-global, but if a jerk is detected at all observatories it is not a proof for a global jerk given the incomplete distribution of surface observatories. Satellite measurements provide complete spatial data coverage and may potentially lead to global identification of geomagnetic jerks. **However, Olsen and Mandea (2007) used these data** to detect a local jerk in 2003 around 90°E and $\pm$ 30° latitude with maximum amplitudes in the radial component. Another local jerk at 2005 around Southern Africa was detected by Olsen and Mandea (2008) using both satellite and observatory data. **A local jerk in 2014 was reported in the ϕ component in the Southern Atlantic-African region (Torta et al., 2015) and in Australia, central Pacific and in Europe (Finlay et al., 2016).** Our results **are in agreement with these findings of local jerks and** suggest that jerks may be indeed confined to some regions, such as in Fig. 11.

The spatial variability of jerk amplitudes may be measured by the ratio between the maxi-

mum and mean amplitudes. In the synthetic time-dependent models the ratio $\mathcal{A}/\mathcal{D}(max)/ < \mathcal{A}/\mathcal{D}(max/4) >$ varies from 1.86 (r component in $\mathcal{P}_2^0(t)$) up to 2.64 (ϕ component in $\mathcal{P}_2^0(t)$). In the 1969 and 1978 geomagnetic jerks the average ratio $< \mathcal{A}/\mathcal{D}(max) > / < \mathcal{A}/\mathcal{D} >$, where the mean applies for each jerk event and each component, reached up to 1.97. This demonstrates that our models encompass a wide range of spatial variability of jerk **amplitude per unit duration time** which is comparable to the corresponding variability observed in geomagnetic data. Note, for example, that in Fig. 8 we observe the three ranges of **amplitude per unit duration time** in a small region around South Africa, with increasing amplitudes to the west. In the model $\mathcal{T}_3^0(t)$ (Fig. 10c) in South America, most jerks are very weak, possibly corresponding to "blind zones" in the geomagnetic data, but there are some intermediate amplitudes that would be detected. This demonstrates that the same jerk event may be detected in some observatories but not detected in neighboring observatories.

Early models of virtual observatories (e.g. Mandea and Olsen, 2006) were biased by external field contributions (Beggan and Whaler, 2009). Recently, Barrois et al. (2018) applied 4-months time binning to improve the removal of external field contributions from virtual observatory time series. In general, after external field removal, jerks in surface observatory data present largest amplitudes in the radial component (e.g. Pinheiro et al., 2011; Brown et al., 2013), in agreement with our results.

We find in nearly all our synthetic models largest **amplitude per unit duration time** in the radial component (Tables 1-2), in agreement with the recent geomagnetic jerks. For example, our $\mathcal{T}_1^0(t)$ flow gives jerk **amplitude per unit duration time** in the r component larger by a factor of ~ 1.5 than in the ϕ component (Table 2). Because our models do not have any external field contribution, it is plausible that indeed a jerk of core origin may have its strongest amplitude in the radial component.

We sampled geomagnetic data of ten surface observatories for the 1969 and 1978 jerks to compare (i) line-segments fit vs. polynomial fits and (ii) the **amplitude per unit duration time** of synthetic models vs. observatory SV time series. Our proposed new polynomial fit to SV time series during jerk events is based on our synthetic models that exhibit smooth changes of sign in the SA. Clearly our core flow models cannot generate abrupt "V-shape" SV changes. While "V-shape" SV changes correspond to regularity of 1.5 (Alexandrescu et al., 1996), our successful third order polynomial fits correspond to regularity 4. However, the differences between the misfits in the line-segments and polynomial fits are small (Figs. 13-14 and Tables 3-4), which may question the definition of geomagnetic jerks as sharp "V-shape" SV trends. Note that somewhat larger misfits in the polynomial fits are expected because of their non-piecewise nature. **We emphasize that both approaches require three fitting parameters only. Two line-segments generally require two fitting parameters each, i.e. four parameters, and likewise the 3rd order polynomial. However, constraining the occurrence time either to the intersection of the two line-segments or to zero SA in the polynomial fit reduces one parameter, leading in practice to three fitting parameters in both approaches.** The small difference between the misfits for the geomagnetic time series with the two methods is therefore rather remarkable. It is probable that the influence of external fields and noise com-

plicates even more the identification of geomagnetic jerks as "V-shape" SV signals. Another possible **prospective** of the new polynomial fit may be to re-calculate differential jerk occurrence times and analyse possible consequences for mantle electrical conductivity modelling (as in Pinheiro and Jackson, 2008).

If the line-segments and polynomial fits would be consistent with each other, $\mathcal{A}$ and $\mathcal{A}/\mathcal{D}$ could be combined to calculate the jerk duration $\mathcal{D}$. In this case, the mean duration times obtained from Tables 3 and 4 would give $\mathcal{D} \sim 4.7$ years, which is obviously large compared with the jerk durations observed in the **geomagnetic** data. This discrepancy is a consequence of the inconsistency between $\mathcal{A}$ of the line-segments method and $\mathcal{A}/\mathcal{D}$ of the third order polynomial fit. In the former $\mathcal{A}$ is constant and $\mathcal{D}$ is zero, whereas in the latter introduced in this study $\mathcal{A}$ and $\mathcal{D}$ are time-dependent but their ratio is constant (14). However, for a given method, comparing amplitudes (or amplitudes per unit duration) of different jerks is sensible.

The mantle electrical conductivity acts as a low-pass filter of core magnetic field variations (Alexandrescu et al., 1996). Pinheiro and Jackson (2008) applied Backus' filter theory for a 1D electrically conducting mantle to a "V-shape" simultaneous jerk at the CMB. They found a delayed and smoothed version of the SV in core. In this case, the mantle electrical conductivity does not change the original jerk amplitude. However, the mantle effect on a non-simultaneous and smooth jerk at the CMB, as in our models, is unknown. Finally, the effect of 3D mantle electrical conductivity models (e.g. Nagao et al., 2003; Velímský and Martinec, 2005) may possibly modify jerk amplitudes.

In summary, we demonstrated that flows with a mild oscillatory time dependence may generate local SV time series with SA changes of sign and reproduce some main observed characteristics of geomagnetic jerks: (i) a range of amplitudes that encompass those observed in geomagnetic jerks, (ii) non-simultaneous occurrence, (iii) non-global occurrence, (iv) spatial variability of amplitudes and (v) strongest amplitudes in the radial component. Our time-dependent flows demonstrate that the flow acceleration does not need to be spatially complex as inferred from SV and SA inversions (e.g. Silva and Hulot, 2012) and the flow does not need to change sign as in torsional oscillations (Bloxham et al., 2002; Cox et al., 2016) in order to reproduce the amplitude of geomagnetic jerks and to explain their spatio-temporal characteristics. Finding the physical mechanism responsible for jerks remains a fundamental challenge for understanding the rapid dynamics of the geodynamo and constraining the physical properties of the mantle.

Acknowledgements

K.J.P. acknowledges the support of Instituto Serrapilheira, Conselho Nacional de Desenvolvimento Científico e Tecnológico (CNPq/Brazil, grant 309884/2016-0) and Fundação de Amparo à Pesquisa do Estado do Rio de Janeiro (FAPERJ/Brazil, grant E-26/202.830/2015). K.J.P. thanks Diana Saturnino for insightful discussions. **We thank two anonymous re-**

viewers for valuable suggestions that helped to improve the manuscript. This work acknowledges financial support from Région Pays de la Loire, project GeoPlaNet (convention no. 2016-10982). This study was also supported by the Centre National des Études Spatiales (CNES). **F.T-N. acknowledges the São Paulo Research Foundation (FAPESP) for grant 2018/07410-3.** We thank INTERMAGNET and the World Data Centre (WDC) for Geomagnetism at the British Geological Survey, for the observatory data used in this study.

References

Alexandrescu, M., Gibert, D., Hulot, G., Mouël, J.-L. L., Saracco, G., 1995. Detection of geomagnetic jerks using wavelet analysis. Journal of Geophysical Research: Solid Earth 100 (B7), 12557–12572, doi:10.1029/95jb00314.

Alexandrescu, M., Gibert, D., Hulot, G., Mouël, J.-L. L., Saracco, G., 1996. Worldwide wavelet analysis of geomagnetic jerks. Journal of Geophysical Research: Solid Earth 101 (B10), 21975–21994, doi:10.1029/96jb01648.

Alexandrescu, M. M., Gibert, D., Mouël, J.-L. L., Hulot, G., Saracco, G., 1999. An estimate of average lower mantle conductivity by wavelet analysis of geomagnetic jerks. Journal of Geophysical Research: Solid Earth 104 (B8), 17735–17745, doi:10.1029/1999jb900135.

Amit, H., Christensen, U. R., 2008. Accounting for magnetic diffusion in core flow inversions from geomagnetic secular variation. Geophysical Journal International 175 (3), 913–924, doi:10.1111/j.1365–246x.2008.03948.x.

Amit, H., Olson, P., 2006. Time-average and time-dependent parts of core flow. Physics of the Earth and Planetary Interiors 155 (1-2), 120–139, doi:10.1016/j.pepi.2005.10.006.

Aubert, J., 2018. Geomagnetic acceleration and rapid hydromagnetic wave dynamics in advanced numerical simulations of the geodynamo. Geophysical Journal International 214 (1), 531–547, doi:10.1093/gji/ggy161.

Aubert, J., Gastine, T., Fournier, A., 2017. Spherical convective dynamos in the rapidly rotating asymptotic regime. Journal of Fluid Mechanics 813, 558–593, doi:10.1017/jfm.2016.789.

Backus, G. E., 1983. Application of mantle filter theory to the magnetic jerk of 1969. Geophys. J. R. Astr. Soc. 74, 713–746.

Balasis, G., Potirakis, S. M., Mandea, M., 2016. Investigating dynamical complexity of geomagnetic jerks using various entropy measures. Frontiers in Earth Science 4, 10.3389/feart.2016.00071.

Barrois, O., Hammer, M. D., Finlay, C. C., Martin, Y., Gillet, N., 2018. Assimilation of ground and satellite magnetic measurements: inference of core surface magnetic and velocity field changes. Geophysical Journal International 215 (1), 695–712, doi:10.1093/gji/ggy297.

740 Beggan, C. D., Whaler, K. A., 2009. Forecasting change of the magnetic field using
741 core surface flows and ensemble kalman filtering. Geophysical Research Letters 36 (18),
742 10.1029/2009gl039927.

743 Beggan, C. D., Whaler, K. A., 2018. Ensemble kalman filter analysis of magnetic field models
744 during the CHAMP-swarm gap. Physics of the Earth and Planetary Interiors 281, 103–110,
745 doi:10.1016/j.pepi.2018.06.002.

746 Bloxham, J., 1986. The expulsion of magnetic flux from the earth's core. Geophys. J. R. astr.
747 Soc. 87, 669–678.

748 Bloxham, J., Zatman, S., Dumberry, M., 2002. The origin of geomagnetic jerks. Nature
749 420 (6911), 65–68, doi:10.1038/nature01134.

750 Brown, W., Mound, J., Livermore, P., 2013. Jerks abound: An analysis of geomagnetic ob-
751 servatory data from 1957 to 2008. Physics of the Earth and Planetary Interiors 223, 62–76,
752 doi:10.1016/j.pepi.2013.06.001.

753 Buffett, B., 2014. Geomagnetic fluctuations reveal stable stratification at the top of the earth's
754 core. Nature 507 (7493), 484–487, doi:10.1038/nature13122.

755 Chambodut, A., Eymin, C., Mandea, M., 2007. Geomagnetic jerks from the earth's surface to
756 the top of the core. Earth, Planets and Space 59 (7), 675–684, doi:10.1186/bf03352730.

757 Chambodut, A., Mandea, M., 2005. Evidence for geomagnetic jerks in comprehensive models.
758 Earth, Planets and Space 57 (2), 139–149, doi:10.1186/bf03352558.

759 Chulliat, A., Maus, S., 2014. Geomagnetic secular acceleration, jerks, and a localized standing
760 wave at the core surface from 2000 to 2010. Journal of Geophysical Research: Solid Earth
761 119 (3), 1531–1543, doi:10.1002/2013jb010604.

762 Chulliat, A., Thébault, E., Hulot, G., 2010. Core field acceleration pulse as a common
763 cause of the 2003 and 2007 geomagnetic jerks. Geophysical Research Letters 37 (7),
764 doi:10.1029/2009gl042019.

765 Constable, S., 2007. Geomagnetism. In: Treatise on Geophysics. Elsevier, pp. 237–276,
766 10.1016/b978–044452748–6.00092–4.

767 Courtillot, V., Ducruix, J., Le-Mouel, J.-L., 1978. Sur une accélération récente de la variation
768 séculaire du champ magnétique terrestre. C. R. Acad. Sci. Paris 287, 1095–1098.

769 Cox, G., Livermore, P., Mound, J., 2016. The observational signature of modelled torsional
770 waves and comparison to geomagnetic jerks. Physics of the Earth and Planetary Interiors
771 255, 50–65, doi:10.1016/j.pepi.2016.03.012.

Cox, G. A., Brown, W. J., Billingham, L., Holme, R., 2018. MagPySV: A python package for processing and denoising geomagnetic observatory data. Geochemistry, Geophysics, Geosystems 19 (9), 3347–3363, doi:10.1029/2018gc007714.

Cox, G. A., Livermore, P. W., Mound, J. E., 2014. Forward models of torsional waves: dispersion and geometric effects. Geophysical Journal International 196 (3), 1311–1329, doi:10.1093/gji/ggt414.

De Michelis, P., Cafarella, L., Meloni, A., 1998. Worldwide character of the 1991 geomagnetic jerk. Earth Planet. Sci. Lett. 25 (3), 377–380.

Demetrescu, C., Dobrica, V., 2014. Multi-decadal ingredients of the secular variation of the geomagnetic field. insights from long time series of observatory data. Physics of the Earth and Planetary Interiors 231, 39–55, doi:10.1016/j.pepi.2014.03.001.

Dormy, E., Mandea, M., 2005. Tracking geomagnetic impulses at the core–mantle boundary. Earth and Planetary Science Letters 237 (1-2), 300–309, doi:10.1016/j.epsl.2005.06.003.

Finlay, C. C., Amit, H., 2011. On flow magnitude and field-flow alignment at earth's core surface. Geophysical Journal International 186 (1), 175–192, doi:10.1111/j.1365–246x.2011.05032.x.

Finlay, C. C., Olsen, N., Kotsiaros, S., Gillet, N., Tøffner-Clausen, L., 2016. Recent geomagnetic secular variation from swarm and ground observatories as estimated in the CHAOS-6 geomagnetic field model. Earth, Planets and Space 68 (1), doi:10.1186/s40623–016–0486–1.

Gillet, N., Jault, D., Canet, E., Fournier, A., 2010. Fast torsional waves and strong magnetic field within the earth's core. Nature 465 (7294), 74–77, doi:10.1038/nature09010.

Gillet, N., Jault, D., Finlay, C. C., Olsen, N., 2013. Stochastic modeling of the earth's magnetic field: Inversion for covariances over the observatory era. Geochemistry, Geophysics, Geosystems 14 (4), 766–786, doi:10.1002/ggge.20041.

Gubbins, D., 1987. Mechanism for geomagnetic polarity reversals. Nature 326 (6109), 167–169, doi:10.1038/326167a0.

Gubbins, D., 2004. Time Series Analysis and Inverse Theory for Geophysicists. Cambridge University Press.

Gubbins, D., Roberts, P. H., 1987. Chapter 1: Magnetohydrodynamics of the Earth's core *in Geomagnetism*. Vol. 2. Academic Press, editor J. A. Jacobs.

Holme, R., 2015. Large-scale flow in the core. In: Olson, P. (Ed.), *Treatise on Geophysics (Second Edition)*. Vol. 8. Elsevier.

Holme, R., de Viron, O., 2013. Characterization and implications of intradecadal variations in length of day. Nature 499 (7457), 202–204, doi:10.1038/nature12282.

Huguet, L., Amit, H., 2012. Magnetic energy transfer at the top of the earth's core. Geophysical Journal International 190 (2), 856–870, doi:10.1111/j.1365–246x.2012.05542.x.

Huy, M. L., Alexandrescu, M., Hulot, G., Mouël, J.-L. L., 1998. On the characteristics of successive geomagnetic jerks. Earth, Planets and Space 50 (9), 723–732, doi:10.1186/bf03352165.

Jackson, A., Jonkers, A. R. T., Walker, M. R., 2000. Four centuries of geomagnetic secular variation from historical records. Philosophical Transactions of the Royal Society of London. Series A: Mathematical, Physical and Engineering Sciences 358 (1768), 957–990, doi:10.1098/rsta.2000.0569.

Johnson, C. L., Constable, C. G., 1997. The time-averaged geomagnetic field: global and regional biases for 0-5 ma. Geophysical Journal International 131 (3), 643–666, doi:10.1111/j.1365–246x.1997.tb06604.x.

Kotzé, P. B., 2017. The 2014 geomagnetic jerk as observed by southern african magnetic observatories. Earth, Planets and Space 69 (1), 10.1186/s40623–017–0605–7.

Malin, S. R. C., Hodder, B. M., 1982. Was the 1970 geomagnetic jerk of internal or external origin? Nature 296, 726–728.

Mandea, M., Bellanger, E., Mouël, J.-L. L., 2000. A geomagnetic jerk for the end of the 20th century? Earth and Planetary Science Letters 183 (3-4), 369–373, doi:10.1016/s0012–821x(00)00284–3.

Mandea, M., Holme, R., Pais, A., Pinheiro, K., Jackson, A., Verbanac, G., 2010. Geomagnetic jerks: Rapid core field variations and core dynamics. Space Science Reviews 155 (1-4), 147–175, doi:10.1007/s11214–010–9663–x.

Mandea, M., Olsen, N., 2006. A new approach to directly determine the secular variation from magnetic satellite observations. Geophysical Research Letters 33 (15), doi:10.1029/2006gl026616.

Maus, S., Silva, L., Hulot, G., aug 2008. Can core-surface flow models be used to improve the forecast of the earth's main magnetic field? Journal of Geophysical Research: Solid Earth 113 (B8), doi:10.1029/2007jb005199.

Merrill, R. T., McElhinney, M. W., McFadden, P. L., 1996. The Magnetic Field of the Earth - Paleomagnetism, the Core, and the Deep Mantle, editor Dmowska, R. and Holton, J. Vol. 63 of International Geophysics Series. Academic Press, San Diago.

838 Michelis, P. D., Cafarella, L., Meloni, A., 2000. A global analysis of the 1991 geo-
839 magnetic jerk. Geophysical Journal International 143 (3), 545–556, doi:10.1046/j.1365–
840 246x.2000.00208.x.

841 Michelis, P. D., Tozzi, R., 2005. A local intermittency measure (LIM) approach to the de-
842 tection of geomagnetic jerks. Earth and Planetary Science Letters 235 (1-2), 261–272,
843 doi:10.1016/j.epsl.2005.04.001.

844 Mouël, J.-L. L., Ducruix, J., Duyen, C. H., 1982. The worldwide character of the 1969–1970
845 impulse of the secular acceleration rate. Physics of the Earth and Planetary Interiors 28 (4),
846 337–350, doi:10.1016/0031–9201(82)90090–5.

847 Nagao, H., Iyemori, T., Higuchi, T., Araki, T., 2003. Lower mantle conductivity anomalies
848 estimated from geomagnetic jerks. Journal of Geophysical Research: Solid Earth 108 (B5),
849 doi:10.1029/2002jb001786.

850 Nagao, H., Iyemori, T., Higuchi, T., Nakano, S., Araki, T., 2002. Local time features of geo-
851 magnetic jerks. Earth, Planets and Space 54 (2), 119–131, doi:10.1186/bf03351712.

852 Olsen, N., Lühr, H., Sabaka, T. J., Mandea, M., Rother, M., Tøffner-Clausen, L., Choi,
853 S., 2006. CHAOS-a model of the earth's magnetic field derived from CHAMP, ørsted,
854 and SAC-c magnetic satellite data. Geophysical Journal International 166 (1), 67–75,
855 doi:10.1111/j.1365–246x.2006.02959.x.

856 Olsen, N., Mandea, M., 2007. Investigation of a secular variation impulse using satellite
857 data: The 2003 geomagnetic jerk. Earth and Planetary Science Letters 255 (1-2), 94–105,
858 doi:10.1016/j.epsl.2006.12.008.

859 Olsen, N., Mandea, M., 2008. Rapidly changing flows in the earth's core. Nature Geoscience
860 1 (6), 390–394, doi:10.1038/ngeo203.

861 Olsen, N., Mandea, M., Sabaka, T. J., Toffner-Clausen, L., 2009. CHAOS-2 - a geomagnetic
862 field model derived from one decade of continuous satellite data. Geophysical Journal Inter-
863 national 179 (3), 1477–1487, doi:10.1111/j.1365–246x.2009.04386.x.

864 Olson, P., Amit, H., 2006. Changes in earth's dipole. Naturwissenschaften 93 (11), 519–542,
865 doi:10.1007/s00114–006–0138–6.

866 Pinheiro, K., Jackson, A., 2008. Can a 1-d mantle electrical conductivity model generate mag-
867 netic jerk differential time delays? Geophysical Journal International 173 (3), 781–792,
868 doi:10.1111/j.1365–246x.2008.03762.x.

869 Pinheiro, K. J., Jackson, A., Amit, H., 2015. On the applicability of backus' mantle filter
870 theory. Geophysical Journal International 200 (3), 1336–1346, doi:10.1093/gji/ggu477.

Pinheiro, K. J., Jackson, A., Finlay, C. C., 2011. Measurements and uncertainties of the occurrence time of the 1969, 1978, 1991, and 1999 geomagnetic jerks. Geochemistry, Geophysics, Geosystems 12 (10), doi:10.1029/2011gc003706.

Poirier, J.-P., 2000. Introduction to the physics of the Earth's interior. Cambridge University Press.

Pozzo, M., Davies, C., Gubbins, D., Alfè, D., 2012. Thermal and electrical conductivity of iron at earth's core conditions. Nature 485 (7398), 355–358, doi:10.1038/nature11031.

Roberts, P. H., Scott, S., 1965. On analysis of the secular variation. J. Geomagn. Geoelectr. 17 (2), 137–151.

Sabaka, T. J., Olsen, N., Purucker, M. E., 2004. Extending comprehensive models of the earth's magnetic field with ørsted and CHAMP data. Geophysical Journal International 159 (2), 521–547, doi:10.1111/j.1365–246x.2004.02421.x.

Schaeffer, N., Jault, D., Nataf, H.-C., Fournier, A., 2017. Turbulent geodynamo simulations: a leap towards earth's core. Geophysical Journal International 211 (1), 1–29, doi:10.1093/gji/ggx265.

Silva, L., Hulot, G., 2012. Investigating the 2003 geomagnetic jerk by simultaneous inversion of the secular variation and acceleration for both the core flow and its acceleration. Physics of the Earth and Planetary Interiors 198-199, 28–50, doi:10.1016/j.pepi.2012.03.002.

Soloviev, A., Chulliat, A., Bogoutdinov, S., 2017. Detection of secular acceleration pulses from magnetic observatory data. Physics of the Earth and Planetary Interiors 270, 128–142, doi:10.1016/j.pepi.2017.07.005.

Stewart, D. N., Whaler, K. A., 1995. Optimal piecewise regression analysis and its application to geomagnetic time series. Geophysical Journal International 121 (3), 710–724, doi:10.1111/j.1365–246x.1995.tb06433.x.

Terra-Nova, F., Amit, H., Hartmann, G. A., Trindade, R. I., Pinheiro, K. J., 2017. Relating the south atlantic anomaly and geomagnetic flux patches. Physics of the Earth and Planetary Interiors 266, 39–53, doi:10.1016/j.pepi.2017.03.002.

Torta, J. M., Pavón-Carrasco, F. J., Marsal, S., Finlay, C. C., 2015. Evidence for a new geomagnetic jerk in 2014. Geophysical Research Letters 42 (19), 7933–7940, doi:10.1002/2015gl065501.

Velímský, J., Martinec, Z., 2005. Time-domain, spherical harmonic-finite element approach to transient three-dimensional geomagnetic induction in a spherical heterogeneous earth. Geophysical Journal International 161 (1), 81–101, doi:10.1111/j.1365–246x.2005.02546.x.

Wardinski, I., Holme, R., 2011. Signal from noise in geomagnetic field modelling: denoising data for secular variation studies. Geophysical Journal International 185 (2), 653–662, doi:10.1111/j.1365–246x.2011.04988.x.

Wardinski, I., Holme, R., Asary, S., Mandea, M., 2008. The 2003 geomagnetic jerk and its relation to the core surface flows. Earth and Planetary Science Letters 267 (3-4), 468–481, doi:10.1016/j.epsl.2007.12.008.